

One-dimensional Luttinger liquids in a two-dimensional moiré lattice

<https://doi.org/10.1038/s41586-022-04514-6>

Received: 16 March 2021

Accepted: 3 February 2022

Published online: 4 May 2022

 Check for updates

Pengjie Wang^{1,10}, Guo Yu^{1,2,10}, Yves H. Kwan^{3,10}, Yanyu Jia¹, Shiming Lei^{4,5}, Sebastian Klemenz^{4,6}, F. Alexandre Cevallos⁴, Ratnadwip Singha⁴, Trithep Devakul⁷, Kenji Watanabe⁸, Takashi Taniguchi⁹, Shivaji L. Sondhi^{1,3}, Robert J. Cava⁴, Leslie M. Schoop⁴, Siddharth A. Parameswaran³ & Sanfeng Wu^{1✉}

The Luttinger liquid (LL) model of one-dimensional (1D) electronic systems provides a powerful tool for understanding strongly correlated physics, including phenomena such as spin–charge separation¹. Substantial theoretical efforts have attempted to extend the LL phenomenology to two dimensions, especially in models of closely packed arrays of 1D quantum wires^{2–13}, each being described as a LL. Such coupled-wire models have been successfully used to construct two-dimensional (2D) anisotropic non-Fermi liquids^{2–6}, quantum Hall states^{7–9}, topological phases^{10,11} and quantum spin liquids^{12,13}. However, an experimental demonstration of high-quality arrays of 1D LLs suitable for realizing these models remains absent. Here we report the experimental realization of 2D arrays of 1D LLs with crystalline quality in a moiré superlattice made of twisted bilayer tungsten ditelluride (tWTe₂). Originating from the anisotropic lattice of the monolayer, the moiré pattern of tWTe₂ hosts identical, parallel 1D electronic channels, separated by a fixed nanoscale distance, which is tuneable by the interlayer twist angle. At a twist angle of approximately 5 degrees, we find that hole-doped tWTe₂ exhibits exceptionally large transport anisotropy with a resistance ratio of around 1,000 between two orthogonal in-plane directions. The across-wire conductance exhibits power-law scaling behaviours, consistent with the formation of a 2D anisotropic phase that resembles an array of LLs. Our results open the door for realizing a variety of correlated and topological quantum phases based on coupled-wire models and LL physics.

In various coupled-wire models^{2–13}, one-dimensional (1D) quantum wires are placed in parallel with each other at an exactly fixed nanoscale distance, producing a two-dimensional (2D) or three-dimensional periodic system. In 2D, such perfectly arranged wires can, in principle, realize a strongly anisotropic non-Fermi liquid phase that resembles a Luttinger liquid (LL)^{2–6}. When a perpendicular magnetic field is applied, new quantum Hall states^{7–9} may also develop in such an array without the presence of a free 2D electron gas. This highly anisotropic setting is qualitatively different from conventional isotropic 2D electron systems. Experimentally realizing these interesting coupled-wire constructions is challenging, as they require a large number of identical nanowires to be strictly arranged in a crystalline array at both nano and microscopic scales. A route to overcome these difficulties is to use moiré superlattices of a twisted bilayer stack of an anisotropic 2D crystal. Indeed, it has been proposed that twisted 2D crystals with a rectangular unit cell, such as GeSe¹⁴, create 1D flat bands. Another excellent choice is tWTe₂, as its monolayer unit cell is an elongated rectangle. In this work, we uncover the potential of tWTe₂ for creating the desired high-quality arrays of 1D wires that can expand the LL physics to 2D.

tWTe₂ moiré lattices and device design

Monolayer WTe₂ consists of three atomic layers (Te–W–Te) in a sandwich structure, in which the W atoms are organized in 1D zigzag chains¹⁵ (Fig. 1a). The tWTe₂ hence has six atomic layers with a complicated moiré pattern. To better illustrate the moiré lattice of small-angle tWTe₂, we present the superlattice of only the W layers and of only the Te layers separately in Fig. 1b, c. The Te pattern develops a triangular superlattice viewed from the top, whereas the W moiré pattern develops 1D stripes, reflecting the underlying anisotropy of the monolayer. The bright stripes in Fig. 1b indicate regions where the W atoms from two layers are optimally aligned vertically (AA stripes), whereas in the dark stripes they are optimally misaligned (AB stripes). The distance d between neighbouring AA stripes depends on the twisted angle θ , $d = a/(2\sin(\theta/2))$, for small θ (Fig. 1d); here a is the length of the monolayer's rectangular unit cell. In Fig. 1e and Extended Data Fig. 1, we experimentally visualize this unique moiré structure of tWTe₂ using conductive atomic force microscopy (cAFM). Below we present transport studies of two devices with $\theta \approx 5^\circ$ ($d \approx 7.2$ nm, device no. 1) and $\theta \approx 6^\circ$ ($d \approx 6.0$ nm, device no. 2).

¹Department of Physics, Princeton University, Princeton, NJ, USA. ²Department of Electrical and Computer Engineering, Princeton University, Princeton, NJ, USA. ³Rudolf Peierls Centre for Theoretical Physics, University of Oxford, Oxford, UK. ⁴Department of Chemistry, Princeton University, Princeton, NJ, USA. ⁵Department of Physics and Astronomy, Rice University, Houston, TX, USA. ⁶Fraunhofer Research Institution for Materials Recycling and Resource Strategies IWKS, Hanau, Germany. ⁷Department of Physics, Massachusetts Institute of Technology, Cambridge, MA, USA. ⁸Research Center for Functional Materials, National Institute for Materials Science, Tsukuba, Japan. ⁹International Center for Materials Nanoarchitectonics, National Institute for Materials Science, Tsukuba, Japan. ¹⁰These authors contributed equally: Pengjie Wang, Guo Yu, Yves H. Kwan. ✉e-mail: sanfengwu@princeton.edu

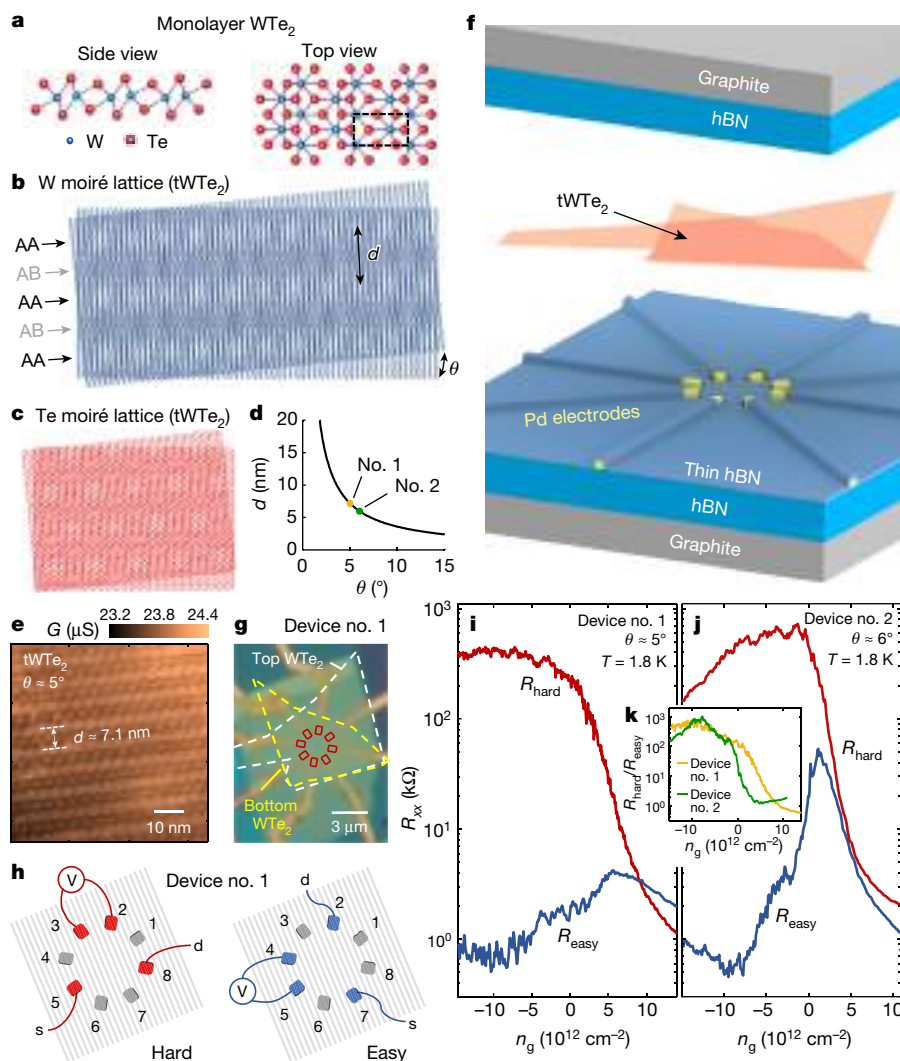


Fig. 1 | Small-angle tWTe₂ moiré lattices and large transport anisotropy. **a**, Crystal structure of monolayer WTe₂ (left: side view; right: top view). The dashed rectangle indicates the unit cell. **b**, Moiré superlattice of W atoms only, showing 1D channels (AA and AB stripes). **c**, Moiré superlattice of the Te atoms, showing a 2D triangular pattern. **d**, Calculated distance d between AA stripes shown in **b**, as a function of twist angle θ . The yellow (green) point indicates the parameter realized in device no. 1 (no. 2). **e**, A cAFM image of the tWTe₂ moiré structure (see details of the measurement in Extended Data Fig. 1 and Methods). **f**, Cartoon illustration of our tWTe₂ device design, in which a thin hBN layer with selectively etched areas is used to avoid electrical contact to non-tWTe₂ regions. **g**, An optical image of device no. 1. The dashed white

(yellow) line highlights the top (bottom) monolayer WTe₂, and the red squares denote the contact regions. **h**, Cartoon illustration of the measurement configuration along hard and easy directions for device no. 1. The grey lines indicate the moiré stripes (not to scale). As an estimation, approximately 71 AA stripes exist between contacts 2 and 3. **s**, source; **d**, drain. **i**, Four-probe resistances measured with configurations shown in **h**, labelled as R_{hard} and R_{easy} , respectively, as a function of n_g for device no. 1 (cooldown no. 1) at 1.8 K. **j**, Similar four-probe resistances along easy and hard directions measured on device no. 2 (cooldown no. 1). **k**, The density-dependent anisotropy ratio, $R_{\text{hard}}/R_{\text{easy}}$, for the two devices, respectively.

Figure 1f illustrates the design of our devices for measuring the transport properties of tWTe₂. Similar to our previous reports^{16,17}, a thin hexagonal boron nitride (hBN) layer is inserted between the tWTe₂ and the palladium (Pd) electrodes, with selected areas etched in the thin hBN layer that expose the very ends of Pd for contacting the tWTe₂ bulk. Such a device geometry restricts the contact area to be small in the 2D bulk and eliminates transport contributions of conducting edges or any extra monolayer regions next to the stack. The tWTe₂ is fully encapsulated with hBN/graphite stacks from both top and bottom, which also act as the electrostatic gates. An optical image of a typical device is shown in Fig. 1g. We fabricate multiple contacts in a ring structure, which is key to investigating transport anisotropy. Details about the fabrication procedure are described in the Methods and Extended Data Fig. 2.

Exceptionally large transport anisotropy

We first examine transport anisotropy in the tWTe₂ devices. Figure 1i shows plots of the four-probe resistance R_{xx} as a function of gate-induced doping n_g , taken from device no. 1 at 1.8 K with the contact configurations (R_{hard} and R_{easy}) shown in Fig. 1h. Here $n_g \equiv \epsilon_r \epsilon_0 (V_{\text{tg}}/d_{\text{tg}} + V_{\text{bg}}/d_{\text{bg}})/e$, where d_{tg} (d_{bg}) is the thickness of hBN dielectric layers for the top (bottom) gate; V_{tg} (V_{bg}) is the top (bottom) gate voltage; e , ϵ_0 and ϵ_r are the elementary charge, vacuum permittivity and relative dielectric constant of hBN, respectively. The current is applied along two orthogonal directions in the atomic plane for measuring R_{hard} and R_{easy} , respectively. The choice of the easy and hard directions was made by comprehensively examining two-probe resistances taken between all neighbouring electrodes and other configurations along and across moiré stripes (Extended Data

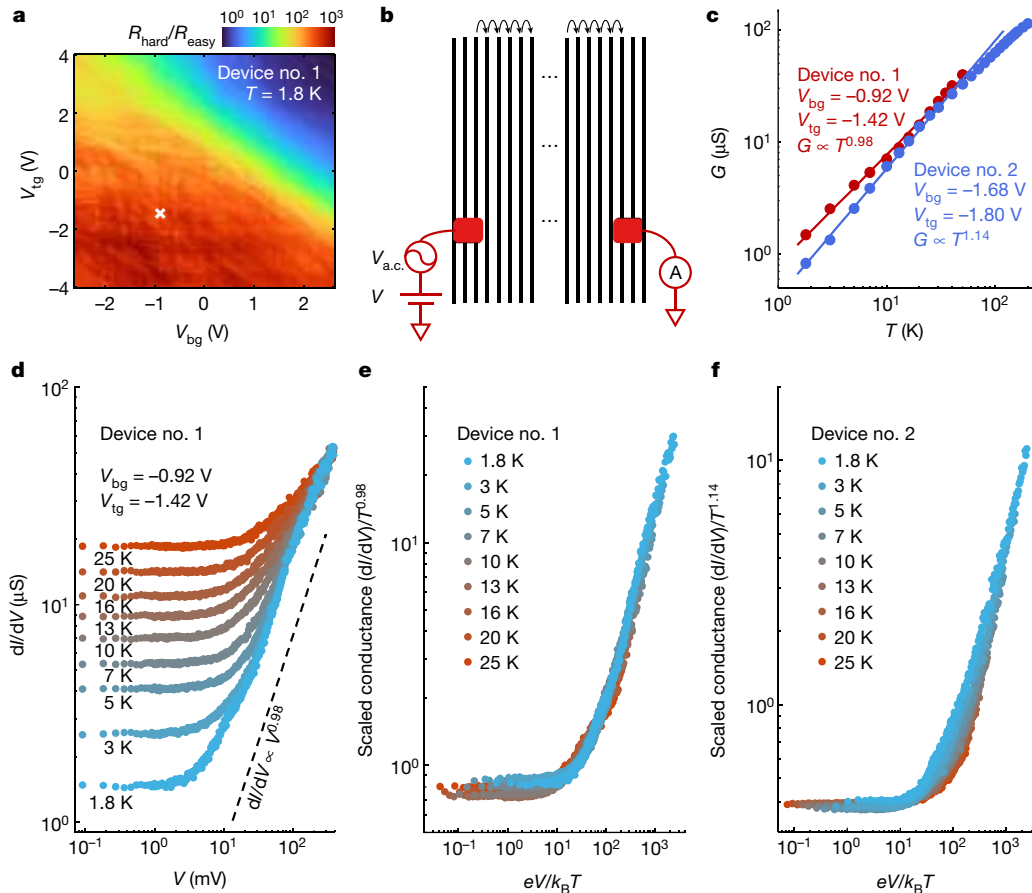


Fig. 2 | Luttinger liquid behaviours observed in the tWTe₂ devices.

a, Dual-gate-dependent map of $R_{\text{hard}}/R_{\text{easy}}$ measured in device no. 1 (cooldown no. 1) at 1.8 K. **b**, Illustration of the measurement configuration for determining two-probe across-wire conductance G and differential conductance dI/dV used in **c–f**. **c**, Across-wire conductance G as a function of T , plotted in log–log scale for device no. 1 (red) and no. 2 (blue) at a selected gate parameter indicated by

the cross in **a**. The solid lines are the power-law fittings. **d**, Across-wire differential conductance dI/dV measured in device no. 1 as a function of d.c. bias V at different T . **e**, The same data as **d**, but plotted as a scaled conductance versus a scaled excitation. All data collapse to a single curve. **f**, The same scaled differential conductance plot taken in the hole-doped regime for device no. 2 (cooldown no. 1), with raw data included in Extended Data Fig. 7.

Fig. 3). The four-probe measurement presented here eliminates the contact resistance and provides a better evaluation of the anisotropy. As seen in Fig. 1i, although R_{hard} and R_{easy} are close when tWTe₂ is electron doped, the two curves substantially deviate from each other when the doping is changed to the hole side. Similar behaviours were also observed in device no. 2 (Fig. 1j and Extended Data Fig. 4). Figure 1k shows plots of the anisotropy ratio, $\beta_{4p} \equiv R_{\text{hard}}/R_{\text{easy}}$, which approaches approximately 1,000 in the hole-doped region, an exceptionally large value. The intrinsic resistivity anisotropy may be estimated to be as large as almost 50 on the basis of an electrostatic simulation considering the effect of measurement geometry (Extended Data Fig. 5).

Both varying the doping to the electron side or warming up the sample (Extended Data Figs. 4 and 6) strongly suppress β_{4p} to near unity, indicating that the large transport anisotropy is an intrinsic low-temperature property of hole carriers. Indeed, the correlation between the anisotropy and the hole doping is clearly seen in Fig. 2a, in which we map out β_{4p} as a function of both V_{tg} and V_{bg} for device no. 1 at 1.8 K (see also Extended Data Fig. 6). The transition from a nearly isotropic phase to a highly anisotropic phase occurs when the hole carriers become dominant, regardless of the electric displacement field.

Conductance power laws

The strongly anisotropic phase of tWTe₂ exhibits robust power-law and scaling behaviours in the across-wire transport (Fig. 2b), in which

currents flow perpendicular to the moiré stripes (that is, the wires). Figure 2c plots the measured across-wire conductance G at a selected gate voltage in the hole-doped regime, with a two-probe configuration shown in Fig. 2b. As seen in the log–log plot, $G \propto T^\alpha$, for T below about 30 K, with an exponent α of approximately 0.98 (or approximately 1.14) for device no. 1 (or no. 2) at the chosen gate voltages. To demonstrate scaling, we present differential conductance (dI/dV) measurements under varying both the d.c. source-drain bias (V) and T (Fig. 2d). For small enough bias, dI/dV develops plateaus, indicating that the conductance is controlled only by T via the power law. At high bias, all curves taken at different T merge together, with a trend that can be well captured by the ‘same’ power-law exponent α , that is, $dI/dV \propto V^\alpha$ (the dashed line). Indeed, in the scaled conductance plot (Fig. 2e), $(dI/dV)/T^\alpha$ versus $eV/k_B T$, all data points, taken in a parameter range wider than a decade in T and three decades in V , collapse into a single curve^{18,19}. A similar collapse can be found in device no. 2 (Fig. 2f and Extended Data Fig. 7).

In Extended Data Fig. 8, we compare along-wire and across-wire conductance taken from device no. 1. More robust power laws are typically seen in the across-wire direction. We note that contact resistance plays an important role in the along-wire transport, as seen in nanotubes¹⁸. In practice, the moiré system in the contact region may be affected by distortions, strain, unintentional doping and other interface effects. By contrast, across-wire resistance at low T is dominated by the tWTe₂ bulk (see Extended Data Fig. 9), a much more uniform area.

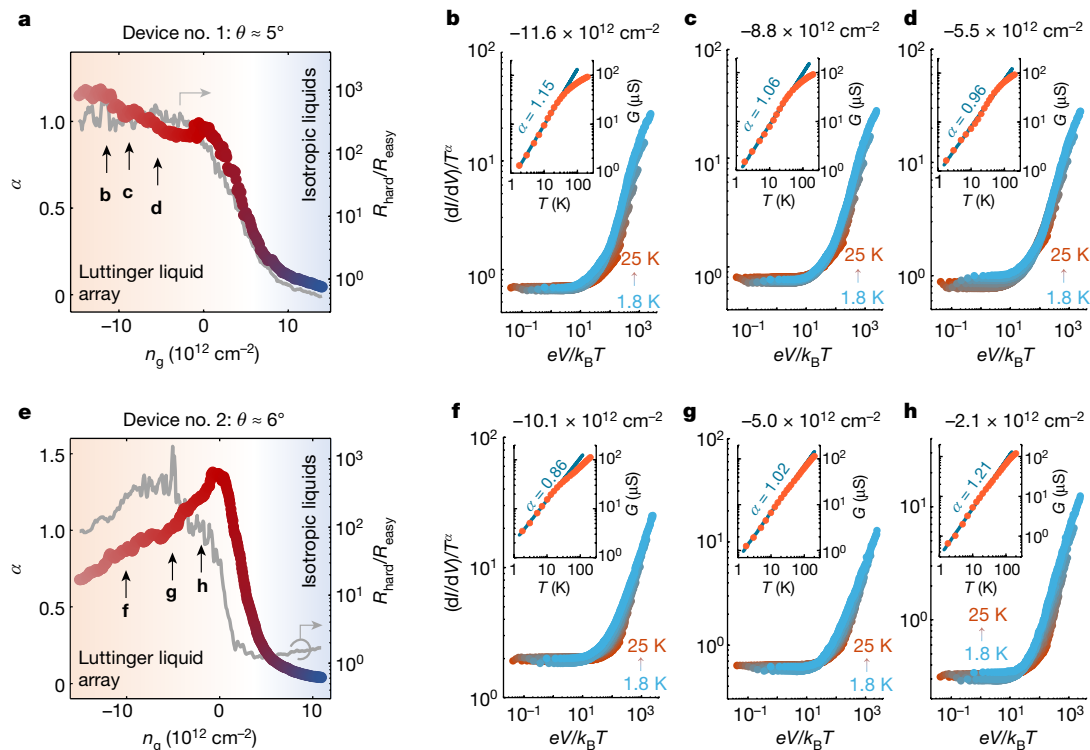


Fig. 3 | Gate-tuned power laws and anisotropy cross-over. **a**, Extracted power-law exponent α as a function of n_g based on temperature-dependent G (raw data in Extended Data Fig. 10), measured in device no. 1 (cooldown no. 2). The grey curve plots the measured anisotropy ratio on the basis of four-probe resistances along the easy and the hard direction in the same cooldown. **b–d**, The scaled differential conductance as a function of $eV/k_B T$ at different n_g ,

indicated in **a**. Insets show the corresponding $G(T)$, from which the corresponding α is extracted on the basis of a power-law fit (solid line) to the low T data. Raw conductance data are shown in Extended Data Fig. 11. **e–h**, The same plots as in **b–d** but for device no. 2 (cooldown no. 2) with raw conductance data shown in Extended Data Figs. 10 and 12.

Gate-tuned anisotropy cross-over

The power-law across-wire conductance is generally observed over a wide range of gate voltages for $T < 30$ K in the tWTe₂ samples, as illustrated in Fig. 3 and Extended Data Figs. 10–12. We extract the n_g -dependent α together with β_{4p} for devices no. 1 and no. 2, respectively (Fig. 3a, e). In the hole-doped side, strong anisotropy occurs together with good power-law scaling characteristics, as shown by the collapse of the dI/dV curves over a wide range of T and V in the scaled plots (Fig. 3b–d for device no. 1; Fig. 3f–h for device no. 2). Although in both devices α is valued near unity on the hole side, the exact gate-dependent behaviour differs, which could arise owing to twist-angle-dependent electronic structures or extrinsic effects, such as disorders. Near charge neutrality or on the electron-doped regime, high-bias data deviate from the power-law trend (Extended Data Figs. 11 and 12). With electron doping, transport anisotropy is strongly suppressed, although zero-bias $G(T)$ still approximately follows a power law with a decreasing exponent down to near zero at high electron doping (Extended Data Fig. 10).

Band structure modelling

We further perform a continuum model analysis on tWTe₂ at the single-particle level (Fig. 4). The modelling is challenging, as even at the monolayer level, topology^{20–23}, correlations^{16,17,24,25} and spin–orbit coupling²⁰ are all present. We start with a density functional theory (DFT) calculation on the monolayer, yielding valence band maximum at Γ flanked by two conduction band minima at the wavevector $\pm q_c$ (Fig. 4a). DFT calculations for untwisted but shifted bilayers are used to extract effective interlayer couplings (Fig. 4b, c), which enter the

continuum model for obtaining the tWTe₂ structure²⁶. The resulting twisted bands arising from one conduction valley are shown in Fig. 4d, in which a pair of highly anisotropic bands indeed develop in the hole regime, in contrast to the electron regime for which no substantial anisotropy is seen. Figure 4f illustrates the corresponding quasi-1D hole Fermi surface with the corresponding real space wavefunctions that coincide with the moiré stripes (Fig. 4e). In contrast to the $\pm q_c$ valleys, the moiré reconstruction of the valence bands at Γ is much less pronounced in this simplified model and develops no large anisotropy (Methods). Note that, although our simple analysis here does capture the emergence of quasi-1D bands, a comprehensive modelling would necessarily require future efforts involving large-scale DFT calculations, lattice reconstructions and interaction effects.

The Luttinger liquid interpretation

The large resistance anisotropy and contrasting T dependence of R_{hard} and R_{easy} (Extended Data Fig. 4) indicate that transport is qualitatively different between across- (insulating) and along-wire (metallic) directions. The power-law behaviour itself is inconsistent with the formation of an ordinary band or Mott insulator. The exponent α varies smoothly as a function of n_g , showing no obvious presence of a fully insulating state (Fig. 3), consistent with the absence of a gap in the modelling. For a 2D diffusive metal^{27,28}, the ‘tunnelling anomaly’ owing to the relaxation of injected charges at the contact may lead to a conductance power law depending on T or V . However, this cannot give distinct transport exponents in different directions and cannot account for our observation along the hard direction, where the resistance is dominated by the tWTe₂ bulk rather than contact effects. For disordered quasi-1D systems, calculations have shown that variable

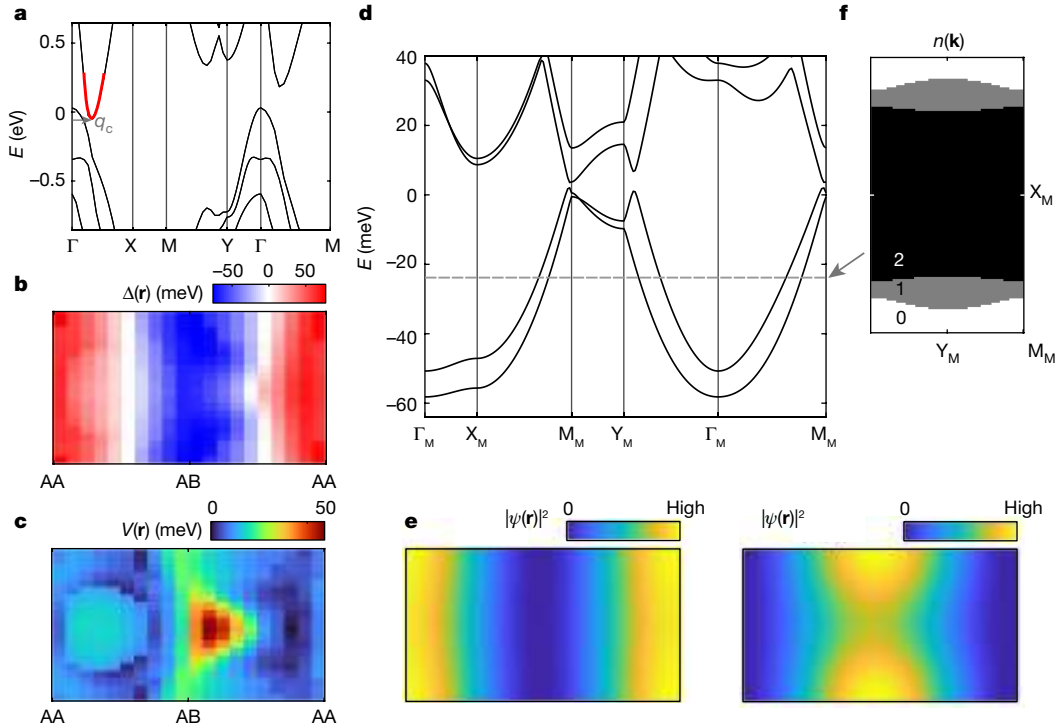


Fig. 4 | Theoretical modelling and the emergence of quasi-1D moiré bands at the single-particle level. **a**, DFT band structure for monolayer WTe₂. Red shading highlights the conduction band valleys at $\pm q_c$, about which the continuum model analysis in **b–f** is performed. Results are shown for one of the valleys. Energies are measured relative to the Fermi energy at charge neutrality. **b,c**, Interlayer hopping (**b**) and potential terms (**c**) plotted in the moiré unit cell. These quantities are extracted from DFT calculations of untwisted bilayers with in-plane shift $\mathbf{d} \approx \theta \hat{z} \times \mathbf{r}$, valid for a rigidly twisted tWTe₂. AA and AB indicate

the positions of W superlattice chains (see Fig. 1b). **d**, Continuum model band structure for a conduction band valley, plotted along a cut in the moiré BZ. On hole doping, the system enters a highly anisotropic regime induced by the moiré physics. **e**, Representative Bloch wavefunctions in the quasi-1D regime plotted in the moiré unit cell. **f**, Illustrations of the quasi-1D open Fermi surfaces for moderate hole doping, with the number of occupied quasi-1D bands indicated.

range hopping transport may produce an apparent power-law behaviour²⁹, that is, $G \propto T^{-\alpha}$ for $eV \ll k_B T$ and $dI/dV \propto V^{-\beta}$ for $k_B T \ll eV$, where α and β are two generally unequal exponents that are independently controlled by microscopic details including disorder. This is, however, in sharp contrast to our observation in tWTe₂, where the power laws in T and V are controlled by the same exponent, namely, $\alpha = \beta$. This single-exponent scaling behaviour is robustly observed over a wide hole-doping range (Fig. 3 and Extended Data Figs. 11 and 12), where α has been tuned, and in samples with varied twist angles (devices no. 1 and no. 2). These observations provide strong evidence that the single-exponent power-law behavior is generic to the anisotropic phase of tWTe₂. Any explanation that requires fine-tuning of parameters to achieve the condition of $\alpha = \beta$ is unlikely to be feasible.

A natural explanation is emergent LL physics. The characteristic feature of a 1D LL in transport is indeed the ‘single-exponent’ power-law dependence of its conductance, that is, $\alpha = \beta$. The power-law transport of LL physics has been observed in several 1D systems, such as nanotubes^{18,19,30,31}, engineered 1D structures^{31–33}, edge modes^{34–36}, polymers³⁷ and self-organized gold wires³⁸. However, extending LL physics from a single 1D wire to a 2D system is of fundamental interest yet challenging. Proposals to do so on the basis of 2D arrays of 1D wires have been put forward^{2–6}, but, as far as we know, the intriguing concept of a 2D anisotropic phase that mimics a LL has so far not been established in real materials.

Our observations on the hole side of tWTe₂ are well consistent with the generic LL expectations. We therefore propose that the anisotropic phase arises because of the formation of a 2D array of 1D LLs induced by the moiré superlattice. Understanding the moiré-induced LL behaviours in tWTe₂ requires proper consideration of electron interactions

and transport mechanisms. In a quasi-1D system, although the early calculations³⁹ of the across-wire transport exponent between parallel LLs indicated $\alpha = 2\eta$, where η (which vanishes without interactions) is the Fermi surface exponent for an individual wire determined by the LL parameter K , the more recent consensus is instead that $\alpha = 2\eta - 1$, where the extra -1 arises from the fact that hopping can occur anywhere along the wires⁴⁰. The relationship applies when single-particle hopping is the dominant conduction process and T is much larger than the 1D to 2D cross-over temperature $T^* \approx t_{\perp}(t_{\parallel}/t_{\perp})^{\eta/(1-\eta)}$, where $t_{\perp}(t_{\parallel})$ is the inter- (intra-) wire hopping⁴⁰. From the energy scales of quasi-1D bands obtained in Fig. 4d, we may estimate $t_{\perp} \approx 5$ and $t_{\parallel} \approx 50$ meV, respectively. If this applies, for certain hole doping of tWTe₂ the across-wire conductance exhibits a power-law exponent $\alpha \approx 1$, corresponding to an effective $\eta \approx 1$, near the marginal boundary above which the single-particle process is no longer relevant and two-particle processes may be important. Assuming spin degeneracy and $\eta = (K + 1/K - 2)/4$ (ref. ⁴⁰), we obtain an effective intrawire $K \approx 0.17$ for $\alpha \approx 1$. The strong intrawire interaction is consistent with the experimental fact that the deviation from the power law is absent down to at least 1.8 K. This remarkably stable LL behaviour in the anisotropic 2D system calls for careful consideration of the interaction-driven phases in tWTe₂, especially the interwire interactions given the nanoscale wire spacing. Considering interwire interactions, the transport exponent then depends on a stiffness function $\kappa(q_{\perp})$ instead of a single intrawire parameter K , where q_{\perp} is the momentum perpendicular to the wires^{3–6}. We note that further experimental and theoretical explorations are necessary to examine the exact connection between the measured power laws to interactions in the system, which is critical to evaluate the enticing possibility of a sliding LL phase and a host of competing orders descending from it^{2–6}.

Summary

We demonstrate a new tuneable platform based on tWTe₂ stacks for studying high-quality 2D arrays of 1D electronic structures in a crystalline superlattice. We interpret the results on the basis of the formation of a 2D anisotropic non-Fermi liquid phase that resembles a LL. An exciting direction is to search for new quantum Hall states with an applied magnetic field^{4,7,8}. The physics of spin–charge separation^{1,31,32}, naturally expected in LLs, is another interesting direction to pursue. Experimental searches for evidence of spin–charge separation in a 2D WTe₂ system could provide important opportunities for studying new regimes in strongly correlated quantum phases.

Online content

Any methods, additional references, Nature Research reporting summaries, source data, extended data, supplementary information, acknowledgements, peer review information; details of author contributions and competing interests; and statements of data and code availability are available at <https://doi.org/10.1038/s41586-022-04514-6>.

- Giamarchi, T. *Quantum Physics in One Dimension* (Oxford Univ. Press, 2003).
- Wen, X. G. Metallic non-Fermi-liquid fixed point in two and higher dimensions. *Phys. Rev. B* **42**, 6623–6630 (1990).
- Emery, V. J., Fradkin, E., Kivelson, S. A. & Lubensky, T. C. Quantum theory of the smectic metal state in stripe phases. *Phys. Rev. Lett.* **85**, 2160–2163 (2000).
- Sondhi, S. L. & Yang, K. Sliding phases via magnetic fields. *Phys. Rev. B* **63**, 054430 (2001).
- Vishwanath, A. & Carpentier, D. Two-dimensional anisotropic non-Fermi-liquid phase of coupled Luttinger liquids. *Phys. Rev. Lett.* **86**, 676–679 (2001).
- Mukhopadhyay, R., Kane, C. L. & Lubensky, T. C. Sliding Luttinger liquid phases. *Phys. Rev. B* **64**, 045120 (2001).
- Kane, C. L., Mukhopadhyay, R. & Lubensky, T. C. Fractional quantum Hall effect in an array of quantum wires. *Phys. Rev. Lett.* **88**, 036401 (2002).
- Teo, J. C. Y. & Kane, C. L. From Luttinger liquid to non-Abelian quantum Hall states. *Phys. Rev. B* **89**, 085101 (2014).
- Tam, P. M. & Kane, C. L. Nondiagonal anisotropic quantum Hall states. *Phys. Rev. B* **103**, 035142 (2021).
- Neupert, T., Chamon, C., Mudry, C. & Thomale, R. Wire deconstructionism of two-dimensional topological phases. *Phys. Rev. B* **90**, 205101 (2014).
- Iadecola, T., Neupert, T., Chamon, C. & Mudry, C. Wire constructions of Abelian topological phases in three or more dimensions. *Phys. Rev. B* **93**, 195136 (2016).
- Meng, T., Neupert, T., Greiter, M. & Thomale, R. Coupled-wire construction of chiral spin liquids. *Phys. Rev. B* **91**, 241106 (2015).
- Patel, A. A. & Chowdhury, D. Two-dimensional spin liquids with Z₂ topological order in an array of quantum wires. *Phys. Rev. B* **94**, 195130 (2016).
- Kennes, D. M., Xian, L., Claassen, M. & Rubio, A. One-dimensional flat bands in twisted bilayer germanium selenide. *Nat. Commun.* **11**, 1124 (2020).

- Ali, M. N. et al. Large, non-saturating magnetoresistance in WTe₂. *Nature* **514**, 205–208 (2014).
- Wang, P. et al. Landau quantization and highly mobile fermions in an insulator. *Nature* **589**, 225–229 (2021).
- Jia, Y. et al. Evidence for a monolayer excitonic insulator. *Nat. Phys.* **18**, 87–93 (2022).
- Bockrath, M. et al. Luttinger-liquid behaviour in carbon nanotubes. *Nature* **397**, 598–601 (1999).
- Yao, Z., Postma, H. W. C., Balents, L. & Dekker, C. Carbon nanotube intramolecular junctions. *Nature* **402**, 273–276 (1999).
- Qian, X., Liu, J., Fu, L. & Li, J. Quantum spin Hall effect in two-dimensional transition metal dichalcogenides. *Science* **346**, 1344–1347 (2014).
- Fei, Z. et al. Edge conduction in monolayer WTe₂. *Nat. Phys.* **13**, 677–682 (2017).
- Tang, S. et al. Quantum spin Hall state in monolayer 1T'-WTe₂. *Nat. Phys.* **13**, 683–687 (2017).
- Wu, S. et al. Observation of the quantum spin Hall effect up to 100 kelvin in a monolayer crystal. *Science* **359**, 76–79 (2018).
- Sajadi, E. et al. Gate-induced superconductivity in a monolayer topological insulator. *Science* **362**, 922–925 (2018).
- Fatemi, V. et al. Electrically tunable low-density superconductivity in a monolayer topological insulator. *Science* **362**, 926–929 (2018).
- Jung, J., Raoux, A., Qiao, Z. & MacDonald, A. H. Ab initio theory of moiré superlattice bands in layered two-dimensional materials. *Phys. Rev. B* **89**, 205414 (2014).
- Levitov, S. & Shytov, A. V. Semiclassical theory of the Coulomb anomaly. *J. Exp. Theor. Phys. Lett.* **66**, 214–221 (1997).
- Bartosch, L. & Kopietz, P. Zero bias anomaly in the density of states of low-dimensional metals. *Eur. Phys. J. B* **28**, 29–36 (2002).
- Rodin, A. S. & Fogler, M. M. Apparent power-law behavior of conductance in disordered quasi-one-dimensional systems. *Phys. Rev. Lett.* **105**, 106801 (2010).
- Ishii, H. et al. Direct observation of Tomonaga–Luttinger-liquid state in carbon nanotubes at low temperatures. *Nature* **426**, 540–544 (2003).
- Deshpande, V. V., Bockrath, M., Glazman, L. I. & Yacoby, A. Electron liquids and solids in one dimension. *Nature* **464**, 209–216 (2010).
- Auslaender, O. M. et al. Spin-charge separation and localization in one dimension. *Science* **308**, 88–92 (2005).
- Sato, Y. et al. Strong electron-electron interactions of a Tomonaga–Luttinger liquid observed in InAs quantum wires. *Phys. Rev. B* **99**, 155304 (2019).
- Glattli, D. C. In *The Quantum Hall Effect: Poincaré Seminar 2004* (eds. Douçot, B. et al.) 163–197 (Birkhäuser, 2005); https://doi.org/10.1007/3-7643-7393-8_5.
- Li, T. et al. Observation of a helical Luttinger liquid in InAs/GaSb quantum spin Hall edges. *Phys. Rev. Lett.* **115**, 136804 (2015).
- Stühler, R. et al. Tomonaga–Luttinger liquid in the edge channels of a quantum spin Hall insulator. *Nat. Phys.* **16**, 47–51 (2020).
- Biermann, S., Georges, A., Giamarchi, T. & Lichtenstein, A. In *Strongly Correlated Fermions and Bosons in Low-Dimensional Disordered Systems* (eds. Lerner, I. V et al.) 81–102 (Springer, 2002); https://doi.org/10.1007/978-94-010-0530-2_5.
- Dudy, L., Aulbach, J., Wagner, T., Schäfer, J. & Claessen, R. One-dimensional quantum matter: gold-induced nanowires on semiconductor surfaces. *J. Phys. Condens. Matter* **29**, 433001 (2017).
- Clarke, D. G., Strong, S. P. & Anderson, P. W. Incoherence of single particle hopping between Luttinger liquids. *Phys. Rev. Lett.* **72**, 3218–3221 (1994).
- Georges, A., Giamarchi, T. & Sandler, N. Interchain conductivity of coupled Luttinger liquids and organic conductors. *Phys. Rev. B* **61**, 16393–16396 (2000).

Publisher's note Springer Nature remains neutral with regard to jurisdictional claims in published maps and institutional affiliations.

© The Author(s), under exclusive licence to Springer Nature Limited 2022

Methods

Sample fabrication

We followed the WTe_2 crystal growth, exfoliation and device fabrication procedures detailed in refs.^{15–17,41}. The stack of tWTe_2 was obtained by the ‘tear and stack’ technique^{42,43}, in which we used the hBN layer to tear and pick up part of a monolayer WTe_2 flake, followed by rotating the rest of the flake counterclockwise by a chosen angle θ and then stacking the two monolayer WTe_2 pieces together. We summarize a step-by-step fabrication process in Extended Data Fig. 2. The device for cAFM measurements consists of a stack of few-layer hBN/ tWTe_2 /hBN on top of a layer of Pd thin film.

Conductive atomic force microscopy measurement

The cAFM measurements⁴⁴ were performed at room temperature in a Bruker Dimension Icon AFM with dry nitrogen purged into the acoustic shield to eliminate the oxygen and water and reduce WTe_2 degradation. A humidity as low as <0.1% and no more than 5% was kept during the measurements. A PF-TUNA module equipped with an in situ current amplifier was used. The device was biased with -2.5 mV d.c. voltage and the d.c. current through the tip was recorded. The 2D conductance image was then captured and plotted, as shown in Extended Data Fig. 1b, c. To better view the moiré pattern, we have applied a standard flatten process and filtered out the 60 Hz electronic noise to the AFM image.

Transport measurement

The electrical measurements of our devices were performed in a cryostat (Quantum Design Dynacool) equipped with a superconducting magnet. Standard lock-in measurements were taken with a frequency of 3–78 Hz. The four-probe measurements were performed by supplying an a.c. current of approximately 3 nA. The two-probe differential conductance measurements were carried out with a small a.c. excitation of 50 or 100 μV , together with a d.c. excitation up to about 400 mV. A current pre-amplifier (DL Instrument 1211) and a voltage pre-amplifier (DL Instrument 1201) were used to improve signals. Two Keithley 2450 source meter units were used to control the top and bottom gates.

Estimating intrinsic anisotropy from four-probe measurements

Following ref.⁴⁵, we discuss the impact that sample geometry and contact placement have on four-probe resistance measurements. In particular, we are interested in how an intrinsic sheet resistivity anisotropy $\beta_{\text{bulk}} = \rho_{xx}/\rho_{yy}$ translates to an observed four-probe anisotropy $\beta_{4p} = R_{xx}/R_{yy}$. We address this by considering the electric potential distribution over the sample in the classical limit. To simplify the problem, we assume that: (1) no current leaks out of the tWTe_2 sample boundary; (2) the sample is characterized by a spatially uniform resistivity tensor $\text{diag}(\rho_0\beta_{\text{bulk}}, \rho_0)$; (3) the external current source/sink distribution $f(x, y)$ is modelled as delta functions at the current contacts; and (4) the voltage (and unused) contacts do not substantially change the physics. By combining the continuity equation, Ohm’s law and Faraday’s law, we obtain an anisotropic Poisson equation for the scalar potential with derivative boundary conditions

$$\left[\frac{1}{\beta_{\text{bulk}}} \partial_x^2 \phi(x, y) + \partial_y^2 \phi(x, y) \right] = -\rho_0 f(x, y)$$

$$\left(\frac{1}{\beta_{\text{bulk}}} \partial_x \phi(x, y), \partial_y \phi(x, y) \right) \cdot \hat{n}_S(x, y) = 0 \quad \text{for } (x, y) \in \partial S$$

where S denotes the tWTe_2 region. From this, the measured resistance can be obtained once the voltage contact locations are prescribed.

We consider a simple caricature of the experimental set-up by taking the sample to be a square of side length L aligned with the principal axes

of the resistivity tensor, that is, the region $[-L/2, L/2] \times [-L/2, L/2]$. For a measurement of R_{xx} , the current contacts are placed at $(\pm L/4, 0)$ and the voltage contacts at $(\pm L/8, L/4)$. R_{yy} is computed similarly, except the contacts are rotated by 90° . The results are shown in Extended Data Fig. 5 for different values of the β_{bulk} . Above some critical value, the measured anisotropy β_{4p} grows exponentially as the square root of β_{bulk} .

Scaling formula and the fitting procedure

To fit the conductance data shown in Fig. 2, we derive a scaling formula for across-wire transport by following the procedure and assumptions in ref.⁴⁶. The resulting formula is:

$$\frac{1}{T^\alpha} \frac{dI}{dV} = A \left[\cosh \gamma x \left[\left(\frac{1+\alpha}{4} \right)^2 + \left(\frac{\gamma x}{2\pi} \right)^2 \right] |\Gamma(z)|^4 + \sinh \gamma x \frac{\gamma x}{2\pi^2} |\Gamma(z)|^4 \right. \\ \left. + \frac{\sinh \gamma x}{\gamma} \left[\left(\frac{1+\alpha}{4} \right)^2 + \left(\frac{\gamma x}{2\pi} \right)^2 \right] \left(\frac{i\gamma}{\pi} |\Gamma(z)|^4 \psi(z) + \text{h.c.} \right) \right]$$

where the dimensionless variable $x = \frac{eV}{2k_B T}$, $z = \frac{1+\alpha}{4} + \gamma \frac{ix}{2\pi}$, $\Gamma(z)$ is the gamma function, $\psi(z)$ is the digamma function, α is the power-law exponent, γ is a constant introduced to account for the division of the source-drain voltage across the multiple wires in series, A is an overall coefficient and h.c. is the Hermitian conjugate. This formula assumes that the dominant transport mechanism between parallel LL channels is single-particle hopping⁴⁶. Note that we have taken a derivative of $I(V)$ to obtain an expression for dI/dV . In the fitting procedure, we first assign the α and $1/\gamma$ to specific values and find the best fit by optimizing the parameter A ; for each combination of α and $1/\gamma$, a root mean squared error (r.m.s.e.) considering all data points is calculated. The r.m.s.e. as functions of α and $1/\gamma$ is plotted as the 2D colour plot (see details in Extended Data Fig. 7 for both device no. 1 and no. 2). The best fits fall in the regions with minimized r.m.s.e. in the 2D plots. We note that our modelling of the tWTe_2 system is at a very early stage at present, and hence new scaling formulae that better describe tWTe_2 transport may be developed in the future, with improved understanding of the system. However, we emphasize that the key experimental demonstration of the power-law scaling here is based on the direct observation of the single-exponent behaviour, that is, $G \propto T^\alpha$ at the low bias limit, $dI/dV \propto V^\alpha$ at the high-bias limit (Fig. 2d) and the fact that all data collapse in the scaled conductance plot (Fig. 2e). These key features are independent of any fitting formula used for analysis.

DFT calculations

DFT calculations on untwisted systems were performed using the plane-wave pseudopotential code QUANTUM ESPRESSO⁴⁷. For the band structure of monolayer WTe_2 , we used fully relativistic optimized norm-conserving Vanderbilt pseudopotentials from PseudoDojo⁴⁸ and the PBE exchange-correlation functional⁴⁹ with a $10 \times 6 \times 1$ k -grid. The van der Waals corrections were included via the semi-empirical framework of DFT-D3 (ref.⁵⁰). The plane-wave cut-off was 80 Ry and Marzari–Vanderbilt smearing of width 0.01 Ry was used. We consider a cell of height 35 Å to eliminate the effect of periodic images. The fully relaxed monolayer geometry was obtained without spin–orbit coupling (SOC) and van der Waals corrections, with a force tolerance of 10^{-4} atomic units on each atom. The shifted untwisted bilayers were constructed by fixing the in-plane positions of the atoms in one of the layers to be displaced by $\mathbf{d} = (dx, dy)$, but letting the out-of-plane coordinates freely relax. The resulting band structures, obtained without SOC, determine the effective interlayer couplings used in the continuum models²⁶. The neglect of SOC in the bilayers is a good approximation, as the band splitting is mostly due to interlayer interactions and is relatively insensitive to SOC. Furthermore, the bands remain spin degenerate, as inversion symmetry is retained for any \mathbf{d} . Although lattice relaxation is not considered, we expect its effect would be important in real devices as it will

deform the heterostructure by expanding the low-energy stackings at the expense of the high-energy regions.

Continuum model calculations

Moiré continuum models can be constructed using input from monolayer and untwisted bilayer DFT data. Doing this for twisted WTe_2 is challenging because (1) the unit cell is rectangular, (2) the (multiple) bands near the Fermi energy are complicated and (3) some of the relevant low-energy features generally lie away from high-symmetry points. This is to be contrasted with hexagonal-based systems, such as graphene (Dirac cones at K), or other transitional metal dichalcogenides (parabolic bands with large band gaps at Γ or K). To make progress, we take the small-angle limit and assume that the main features of monolayer WTe_2 can be treated separately (that is, the valence band maximum and conduction band minima (valleys)). Although these bands have significant energetic overlap, for small twist angles and smooth moiré potentials the coupling between these bands will be suppressed.

The general approach is to first model an effective Bloch Hamiltonian $H(\mathbf{k}, \mathbf{d})$ that describes the untwisted bilayer for different in-plane shifts \mathbf{d} (it is assumed here that the out-of-plane coordinates have been relaxed)²⁶. This typically involves kinetic energy terms $E(\mathbf{k})$ from the individual layers, as well as (layer-dependent) interlayer potential $V(\mathbf{k}, \mathbf{d})$ and hopping terms $\Delta(\mathbf{k}, \mathbf{d})$. If we take one band from each layer, the effective Hamiltonian is

$$H(\mathbf{k}, \mathbf{d}) = \begin{pmatrix} E(\mathbf{k}) + V_b(\mathbf{k}, \mathbf{d}) & \Delta(\mathbf{k}, \mathbf{d}) \\ \Delta^*(\mathbf{k}, \mathbf{d}) & E(\mathbf{k}) + V_t(\mathbf{k}, \mathbf{d}) \end{pmatrix}$$

where $\Delta^*(\mathbf{k}, \mathbf{d})$ is the complex conjugation of $\Delta(\mathbf{k}, \mathbf{d})$. Then the relation $\mathbf{d} \approx \theta \hat{z} \times \mathbf{r}$, valid for rigid twists, is used to convert the interlayer interactions into ‘hopping’ terms in the moiré reciprocal lattice. Note that, depending on the momentum base point, the twist will also induce a relative difference between the kinetic terms in the two layers. In particular, the conduction valley continuum model is based at q_c , which is around one-third the distance to the Brillouin zone boundary in the a direction. The resulting matrix (in combined band/layer/moiré reciprocal lattice vector space) is diagonalized with a large enough plane-wave cut-off to ensure convergence in the energy window of interest.

We apply the approach above to obtain the reconstructed moiré bands from a conduction band valley. SOC is neglected (as in the bilayer DFT calculations) and spin degeneracy is assumed (inversion is only weakly broken for small twists). The kinetic terms are taken as effective mass parabolas to emulate the band extrema in the monolayer: $m_x = m_y = 0.38m_e$ for the valleys. The interlayer interactions $V(\mathbf{d})$ and $\Delta(\mathbf{d})$ are taken to be independent of momentum. This is justified if the relevant momentum region is small, as these quantities are already finite at the base point momenta. The symmetries of the monolayer, namely inversion, mirror and time-reversal, can be used to constrain the \mathbf{d} dependence of the interlayer quantities, which are fit to the energy shift and splitting of the bilayer DFT bands at the base point momenta. The results are shown in Fig. 4. We further note that, whereas the conduction valleys show a pronounced anisotropy on the hole side, the continuum bands at the valence maximum do not show obvious signs of appreciable quasi-1D behaviour in our modelling. On one hand, carriers originated from the valence maximum may be localized in real devices. This may be evidenced by the fact that the transport of monolayer WTe_2 is known to exhibit less mobility for hole doping compared to electron doping. On the other hand, we emphasize that more complete modelling is necessary for the development of a comprehensive understanding of the tWTe_2 moiré system. For example, the continuum model parameters were extracted by assuming a rigid rotation

between two monolayers. It is known, however, that lattice relaxation and corrugation effects can be significant for small twist-angle moiré heterostructures^{51,52}. Electron interactions are also expected to play an important role in the system. Although the general prediction here of moiré-induced quasi-1D features should be robust, to obtain a more comprehensive picture of the twisted band structure it is crucial to perform large-scale, fully relaxed DFT calculations on tWTe_2 and to consider electron interactions and SOC properly.

Data availability

The data that support the findings of this study are available at Harvard Dataverse (<https://doi.org/10.7910/DVN/PFXXSZ>) or from the corresponding author upon reasonable request.

- Ali, M. N. et al. Correlation of crystal quality and extreme magnetoresistance of WTe_2 . *Europhys. Lett.* **110**, 67002 (2015).
- Kim, K. et al. Tunable moiré bands and strong correlations in small-twist-angle bilayer graphene. *Proc. Natl Acad. Sci. USA* **114**, 3364–3369 (2017).
- Cao, Y. et al. Unconventional superconductivity in magic-angle graphene superlattices. *Nature* **556**, 43–50 (2018).
- Ponomarenko, L. A. et al. Cloning of Dirac fermions in graphene superlattices. *Nature* **497**, 594–597 (2013).
- Simon, S. H. Comment on “Evidence for an anisotropic state of two-dimensional electrons in high Landau levels”. *Phys. Rev. Lett.* **83**, 4223–4223 (1999).
- Lopatin, A., Georges, A. & Giamarchi, T. Hall effect and interchain magneto-optical properties of coupled Luttinger liquids. *Phys. Rev. B* **63**, 075109 (2001).
- Giannozzi, P. et al. Advanced capabilities for materials modelling with Quantum ESPRESSO. *J. Phys. Condens. Matter* **29**, 465901 (2017).
- van Setten, M. J. et al. The PseudoDojo: training and grading a 85 element optimized norm-conserving pseudopotential table. *Comput. Phys. Commun.* **226**, 39–54 (2018).
- Perdew, J. P., Burke, K. & Ernzerhof, M. Generalized gradient approximation made simple. *Phys. Rev. Lett.* **77**, 3865–3868 (1996).
- Grimme, S., Antony, J., Ehrlich, S. & Krieg, H. A consistent and accurate ab initio parametrization of density functional dispersion correction (DFT-D) for the 94 elements H–Pu. *J. Chem. Phys.* **132**, 154104 (2010).
- Naik, M. H. & Jain, M. Ultraflatbands and shear solitons in moiré patterns of twisted bilayer transition metal dichalcogenides. *Phys. Rev. Lett.* **121**, 266401 (2018).
- Nam, N. N. T. & Koshino, M. Lattice relaxation and energy band modulation in twisted bilayer graphene. *Phys. Rev. B* **96**, 075311 (2017).

Acknowledgements We acknowledge discussions with N. P. Ong, A. Yazdani, B. A. Bernevig, F. H. L. Essler, B. Lian, C. Kane, K. Yang, A. J. Uzan, Y. Werman and J. Zhang. We thank S. H. Simon for discussions and for pointing out ref. ⁴⁵ to us. This research was supported by NSF through a CAREER award to S.W. (DMR-1942942) and the Princeton University Materials Research Science and Engineering Center (DMR-2011750) through support to S.W., R.J.C. and L.M.S. Device characterization and data analysis were partially supported by ONR through a Young Investigator Award (N00014-21-1-2804) to S.W. S.W. and L.M.S. acknowledge support from the Eric and Wendy Schmidt Transformative Technology Fund at Princeton. Early measurements were performed at the National High Magnetic Field Laboratory, which is supported by NSF Cooperative Agreement no. DMR-1644779 and the State of Florida. K.W. and T.T. acknowledge support from the Elemental Strategy Initiative conducted by the MEXT, Japan, grant number JPMXP0112101001, JSPS KAKENHI grant number JP20H00354 and the CREST (JPMJCR15F3), JST. L.M.S. acknowledges support from the Gordon and Betty Moore Foundation’s EPIQS initiative through grant no. GBMF9064 to L.M.S., the David and Lucile Packard Foundation, the Sloan Foundation and Princeton’s catalysis initiative. Y.H.K. and S.A.P. acknowledge support from the European Research Council under the European Union’s Horizon 2020 Research and Innovation Programme via grant agreement no. 804213-TMCS. S.L.S. was supported by the Gordon and Betty Moore Foundation through grant no. GBMF8685 towards the Princeton theory program and by a Leverhulme International Professorship at Oxford.

Author contributions S.W. conceived and designed the project. P.W. and G.Y. fabricated devices, performed measurement and analysed data, assisted by Y.J. and supervised by S.W. Y.H.K., T.D., S.L.S. and S.A.P. performed theoretical modelling. F.A.C., R.J.C., S.L., S.K., R.S. and L.M.S. grew and characterized bulk WTe_2 crystals. K.W. and T.T. provided hBN crystals. S.W., P.W., S.A.P. and Y.H.K. wrote the paper with input from all authors.

Competing interests The authors declare no competing interests.

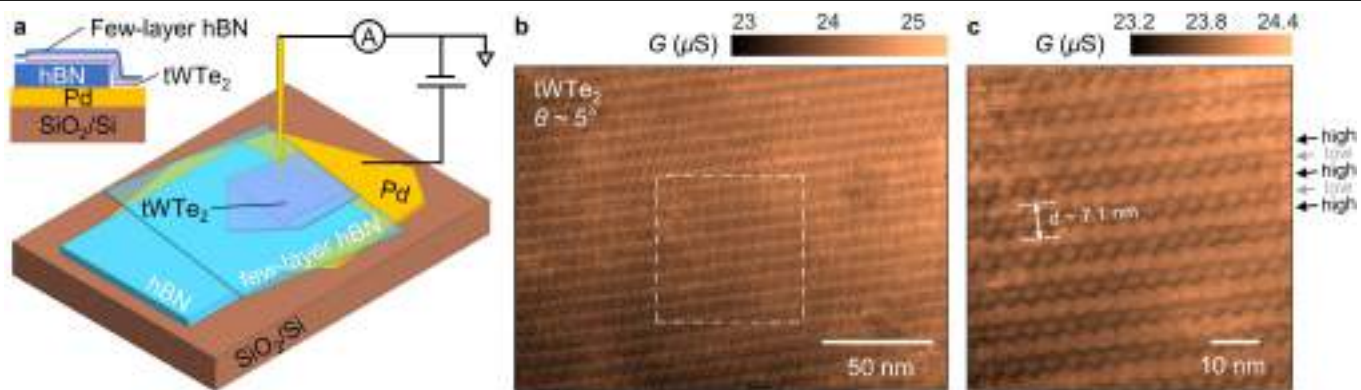
Additional information

Supplementary information The online version contains supplementary material available at <https://doi.org/10.1038/s41586-022-04514-6>.

Correspondence and requests for materials should be addressed to Sanfeng Wu.

Peer review information *Nature* thanks Dante Kennes and the other, anonymous, reviewer(s) for their contribution to the peer review of this work.

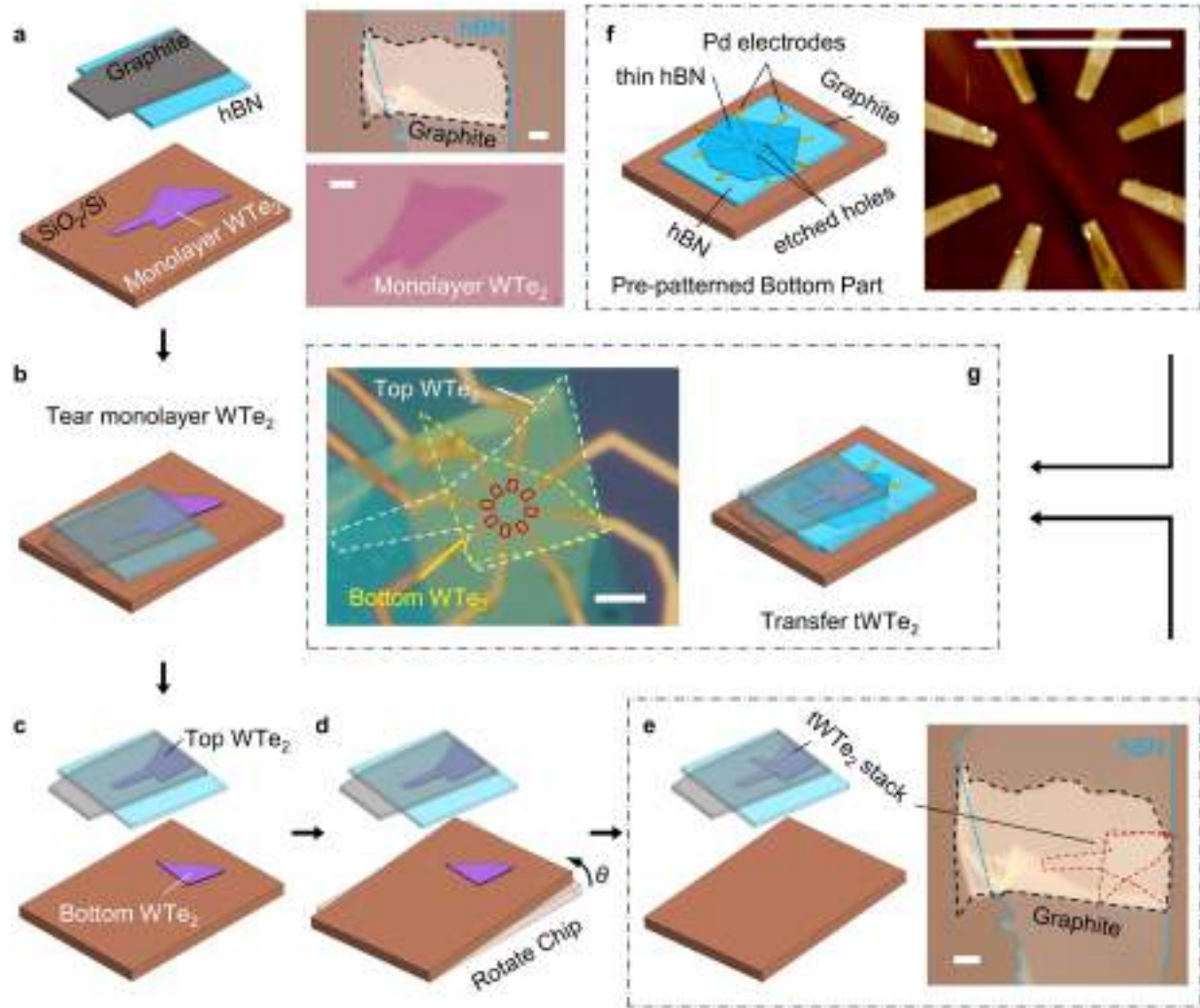
Reprints and permissions information is available at <http://www.nature.com/reprints>.



Extended Data Fig. 1 | Conductive atomic force microscope (cAFM)

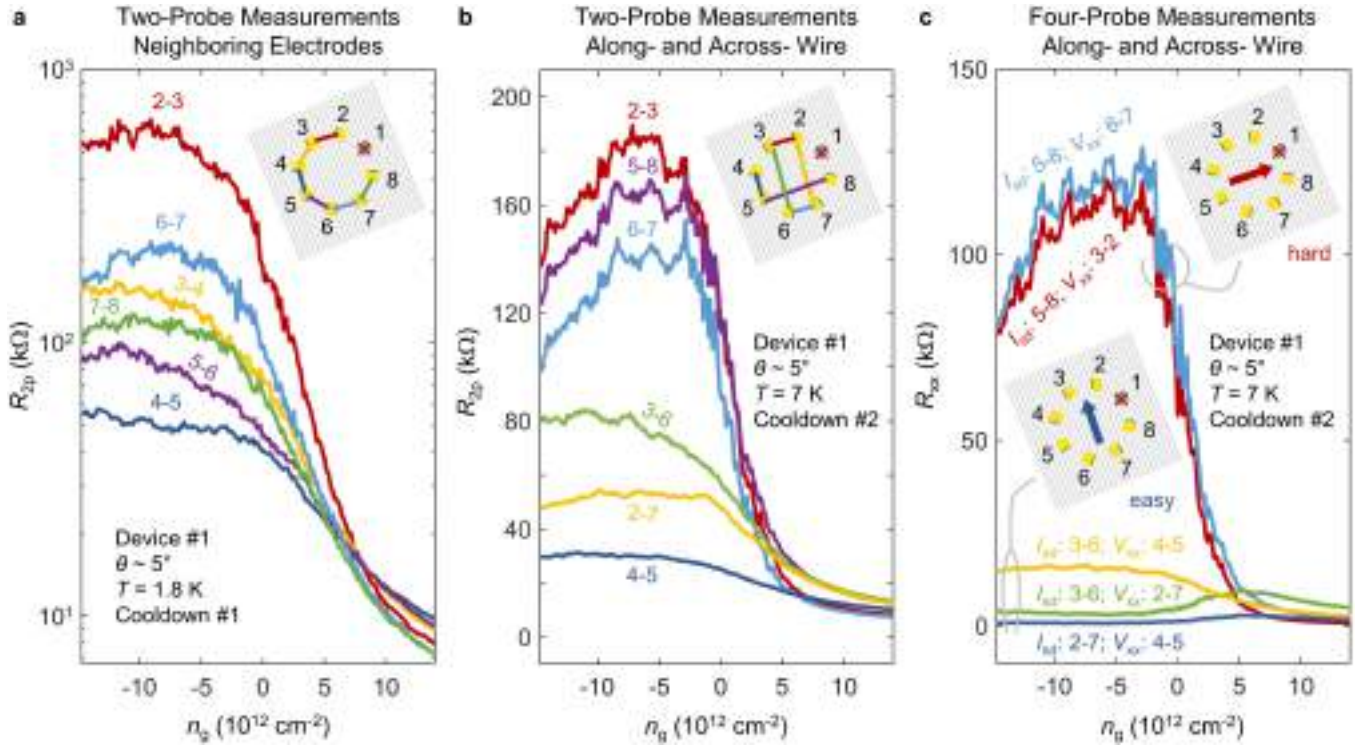
measurements of tWTe₂ at room temperature. **a**, Cartoon illustrations of the cAFM measurement on a few-layer hBN/tWTe₂/hBN stack on a Pd metal film pre-patterned on a SiO₂/Si chip. The inset illustrates the cross-section of the stack. A relatively thick (around 39 nm) hBN was used to mitigate the roughness of the metal surface. **b**, A cAFM image taken from a $\theta \approx 5^\circ$ tWTe₂ device, directly visualizing the moiré structure. The dashed-dot square locates a zoom-in scan, as shown in **c**. We comment on three aspects of the observations. (1) The measurement was taken at room temperature, where the transport shows no significant anisotropy. This is consistent with the fact the measured local conductance G varies only by a small amount at different tip locations in the map. (2) As shown in **b** and **c**, the small variations already allow us to clearly image the underlying moiré structure. (3) Our experimental resolution does

not allow us to identify which one is the AA stripe or the AB stripe, but the map is clearly consistent with the pattern shown in Fig 1b, except with lattice relaxations. The relatively low and high conductance regions develop into stripes, with an inter-stripe distance approximately 7.1 nm, consistent with the expectation for a $\theta \approx 5^\circ$ tWTe₂ stack. (4) As WTe₂ is air sensitive, we have to use a few-layer hBN as a protecting layer and a sample fabrication process that minimizes the time for the sample exposed to air. The top surface of the thin hBN is left behind with polymer residues etc, which we believe could be the main source of the residue-like features in **b** and **c**. Our transport devices (devices no. 1 & no. 2 in the main text) use a top graphite gate that serves as a screening layer and hence the tWTe₂ channel is of much higher quality. Other details about the cAFM measurements can be found in the Methods.



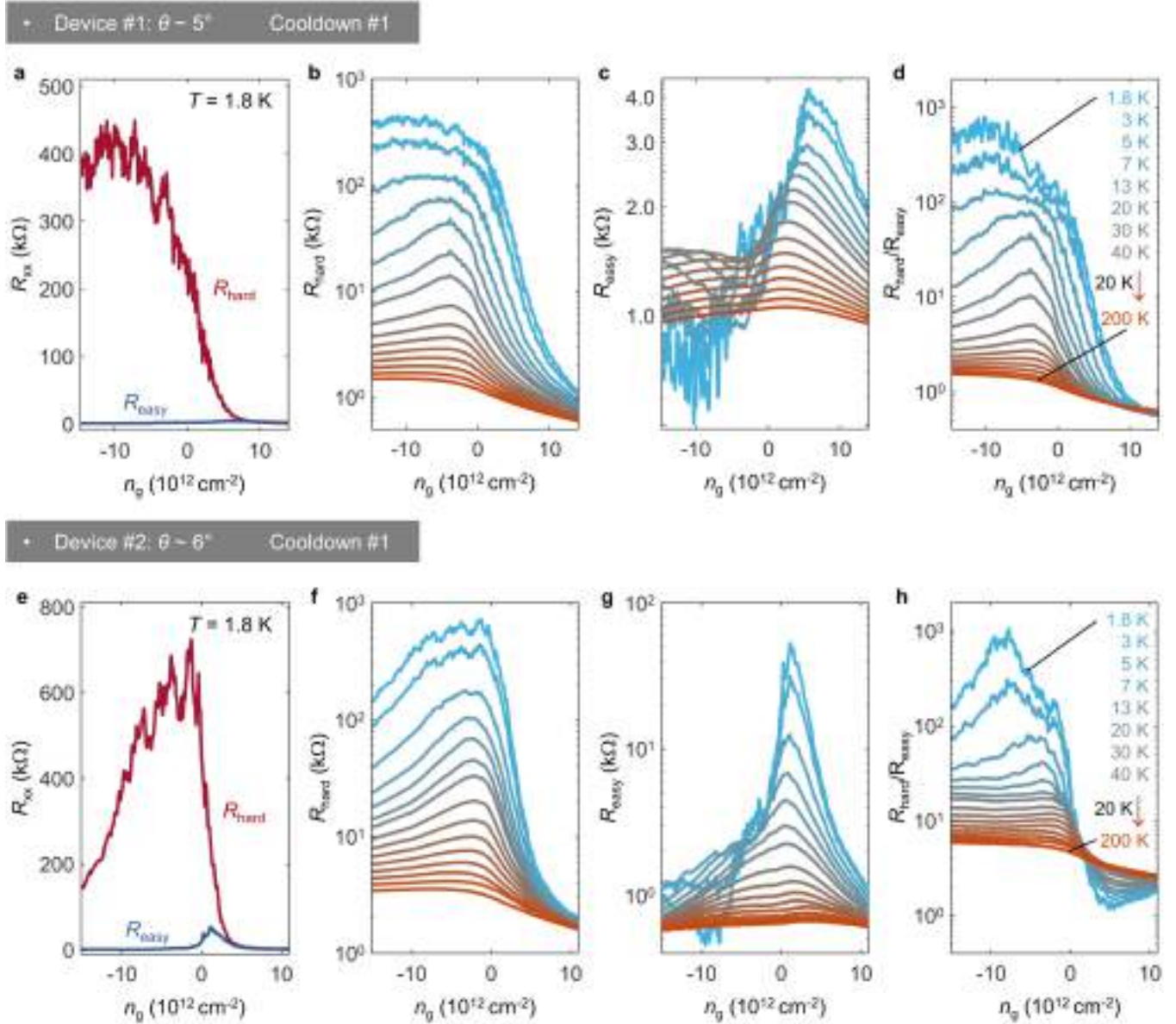
Extended Data Fig. 2 | Sample fabrication process. **a**, Cartoon illustrations of a prepared top graphite/hBN stack (top) and a flake of monolayer WTe_2 on a SiO_2/Si chip (bottom). Their corresponding optical images are also shown to the right. The distance between the aligned graphite edge and hBN edge is carefully optimized during transfer to be within 500 nm. **b & c**, Tear the monolayer WTe_2 by the hBN into two separate pieces, labelled as top and bottom WTe_2 . **d**, Rotate the bottom WTe_2 flake, i.e., the SiO_2/Si chip, counterclockwise by θ . **e**, Pick up the bottom WTe_2 to create a tWTe_2 stack. The optical image of the tWTe_2 stack shown to the right was taken after flipping the stamp upside down. The tWTe_2 stack is highlighted by the red dashed line.

No visible bubbles were observed. **f**, The pre-patterned bottom part (thin hBN/Pd electrodes/hBN dielectric/graphite) with etched holes in the thin hBN layer to expose the tips of the Pd electrodes (see ref. ^{16,17}). An atomic force microscope image shows a clean surface of a prepared bottom stack. **g**, The final stack of a tWTe_2 device, with an optical image of a final device (no. 1). The thickness of flakes is 7.6 nm graphite/8.9 nm top hBN/ WTe_2 /2.0 nm thin hBN/5.5 nm bottom hBN/7.0 nm graphite for device no. 1 and 4.8 nm graphite/10.6 nm top hBN/ WTe_2 /4.2 nm thin hBN/15.0 nm bottom hBN/6.9 nm graphite for device no. 2. All scale bars are 3 μm .



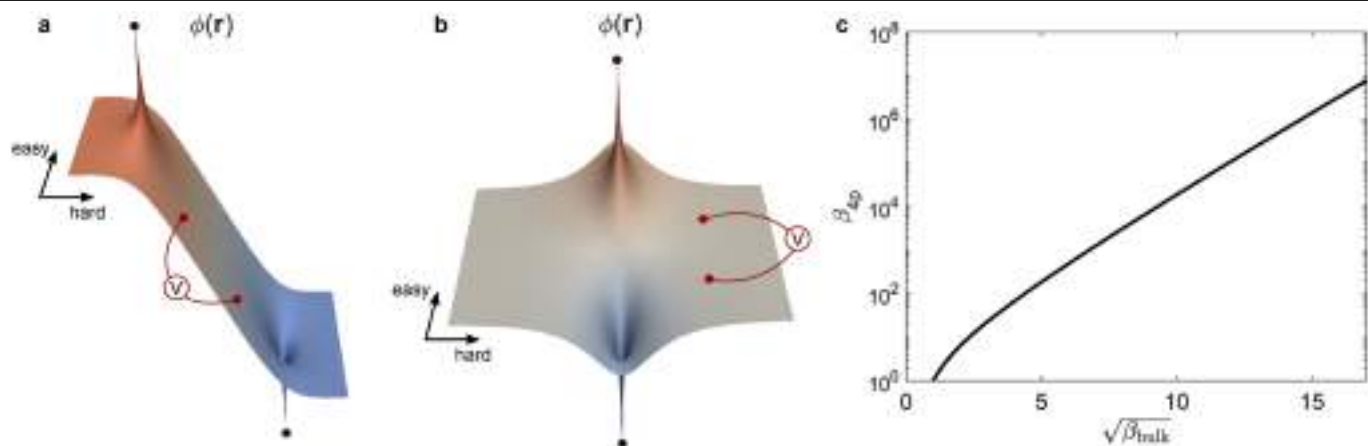
Extended Data Fig. 3 | More analysis on the transport anisotropy on device no. 1. **a**, Two-probe resistance between neighbouring electrodes as a function of n_g in cooldown no. 1. Inset shows the contact configurations for each measurement, where the estimated hard direction (stripe direction) is indicated by the grey lines (not to scale). $R_{2,3}$ and $R_{6,7}$ display larger values than all others in the hole-doped regime, signifying the hard direction, whereas $R_{4,5}$ shows the lowest value. Contact 1 was broken during the fabrication. The contact resistance plays a significant role here. After the easy and hard

directions were identified, we performed four-probe measurements, as shown in Fig. 1 in the main text.). **b**, Two-probe resistance across ($R_{2,3}$, $R_{6,7}$, and R_{5-8}) and along ($R_{4,5}$, R_{2-7} , and R_{3-6}) the stripes as a function of n_g in cooldown no. 2. Inset shows the contact configurations for each measurement, where the easy direction (along stripes) is indicated by the grey lines (not to scale). **c**, Four-probe resistance across ($I_{sd}: 5-8; V_{xx}: 6-7$ and $I_{sd}: 5-8; V_{xx}: 3-2$) and along ($I_{sd}: 3-6; V_{xx}: 4-5$, $I_{sd}: 3-6; V_{xx}: 2-7$, and $I_{sd}: 2-7; V_{xx}: 4-5$) the stripes as a function of n_g in cooldown no. 2.



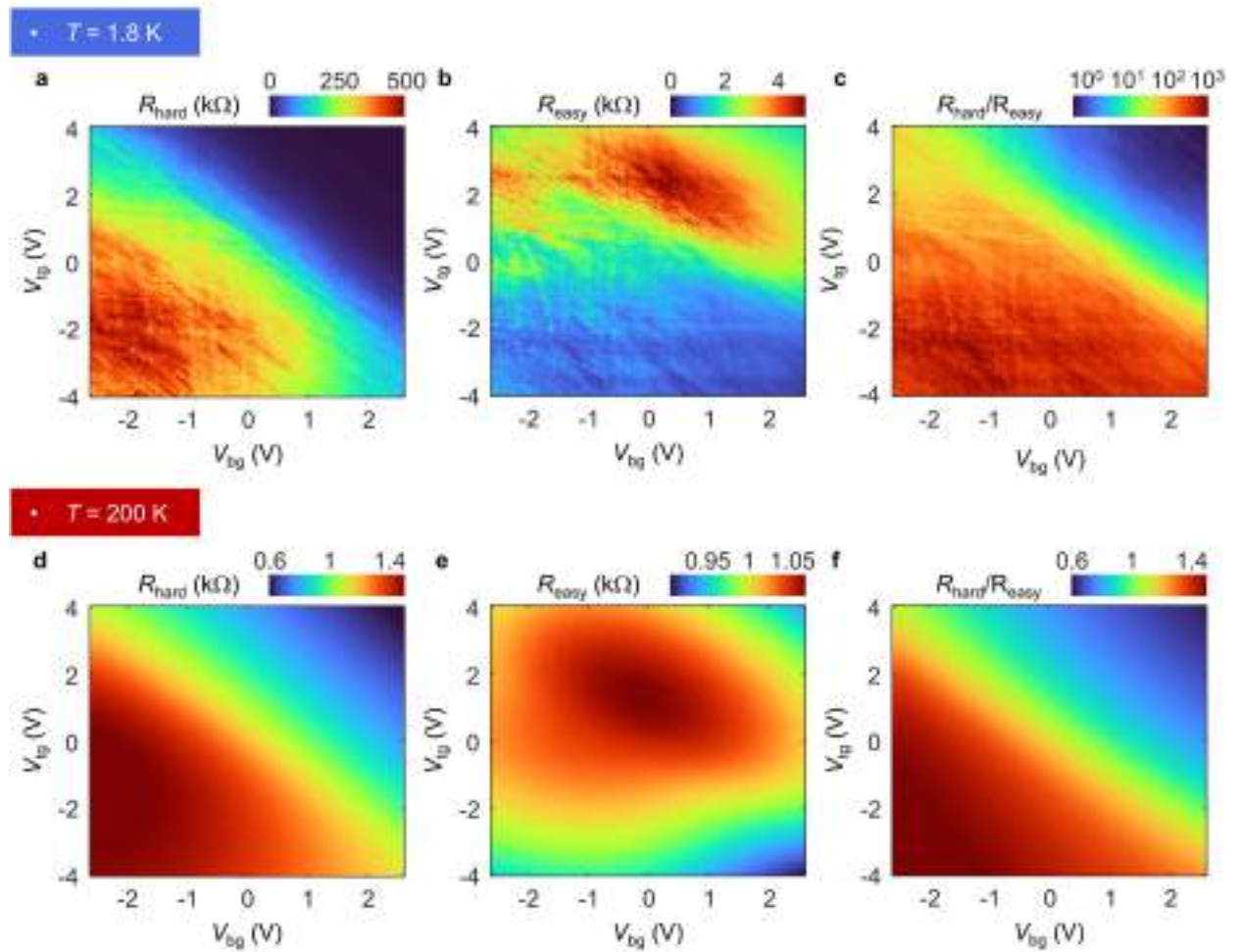
Extended Data Fig. 4 | n_g dependent transport anisotropy for devices no. 1 and no. 2. Four-probe resistance R_{xx} as a function of n_g measured with an excitation current applied along hard and easy directions in linear plots. **a**, data

taken for device no. 1 at 1.8 K (the same data as Fig. 1i). **b-d**, R_{hard} , R_{easy} , and R_{hard}/R_{easy} as a function of n_g at different temperatures taken from device no. 1. **e-h**, The same plots for device no. 2.



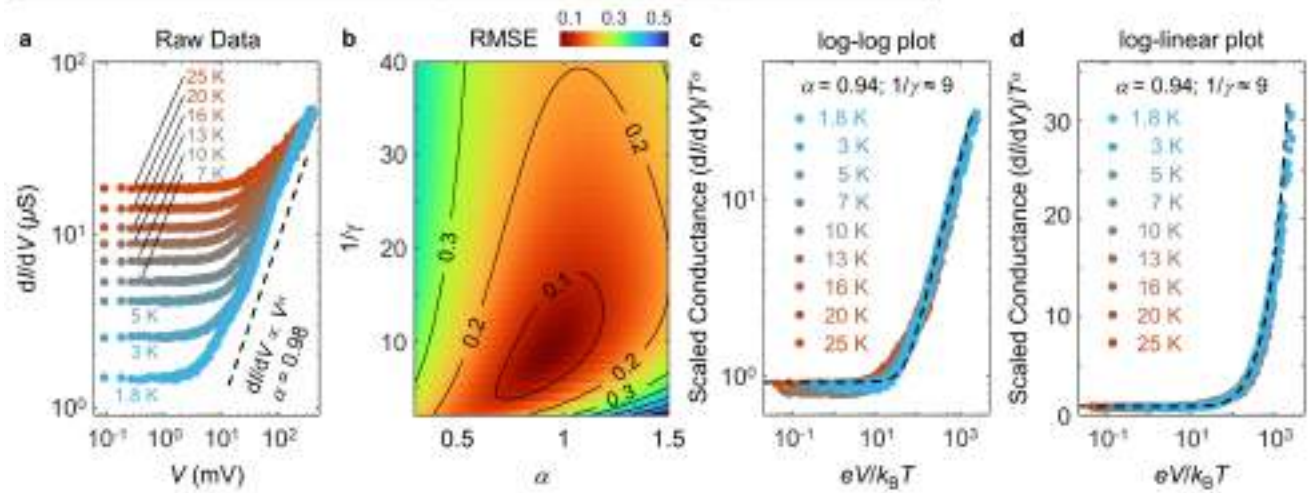
Extended Data Fig. 5 | Electrostatic simulation for the four-probe contact configuration. a & b, Electric potential distribution for contact arrangements corresponding to R_{hard} and R_{easy} four-probe measurements respectively (see Methods). Black dots indicate current contacts that source/sink current. Red

dots indicate the placement of voltage contacts. **c,** Predicted four-probe anisotropy $\beta_{4p} \equiv R_{\text{hard}}/R_{\text{easy}}$ as a function of the intrinsic sheet resistivity anisotropy β_{bulk} . For $\beta_{4p} \approx 1,000$, we estimate $\beta_{\text{bulk}} \approx 50$.

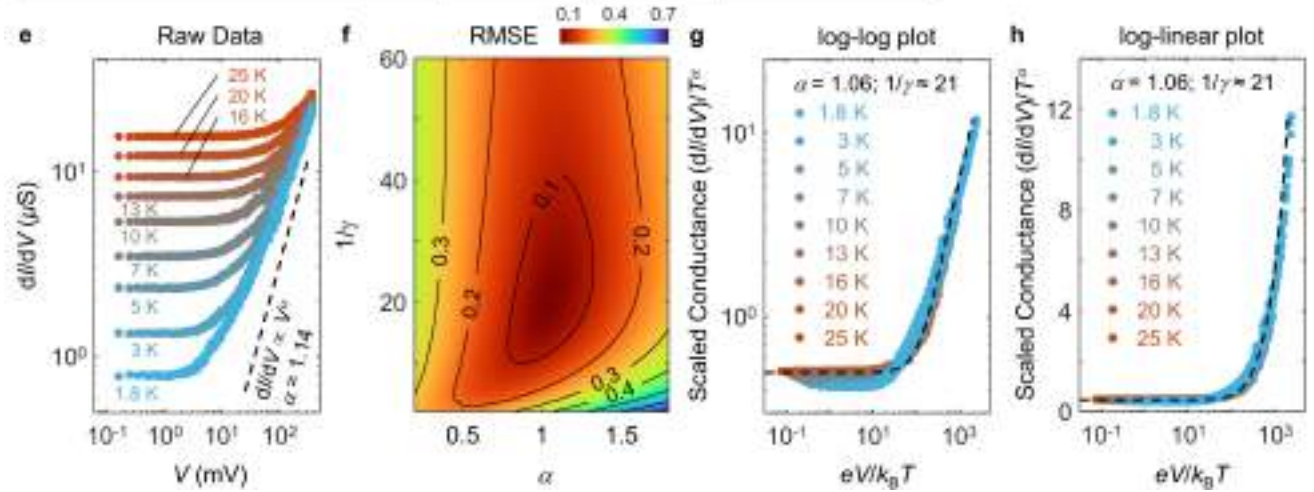


Extended Data Fig. 6 | Dual-gate-dependent transport along hard and easy directions (device no. 1, cooldown no. 1). The four-probe resistance taken at 1.8 K (200 K) along the hard and easy directions were shown in **a** (**d**) and **b** (**e**), respectively. $R_{\text{hard}}/R_{\text{easy}}$ at 1.8 K (200 K) is shown in **c** (**f**).

• Device #1 Cooldown #1 $V_{\text{bg}} = -0.92 \text{ V}$; $V_{\text{g}} = -1.42 \text{ V}$; $n_0 = -5.5 \times 10^{12} \text{ cm}^{-2}$

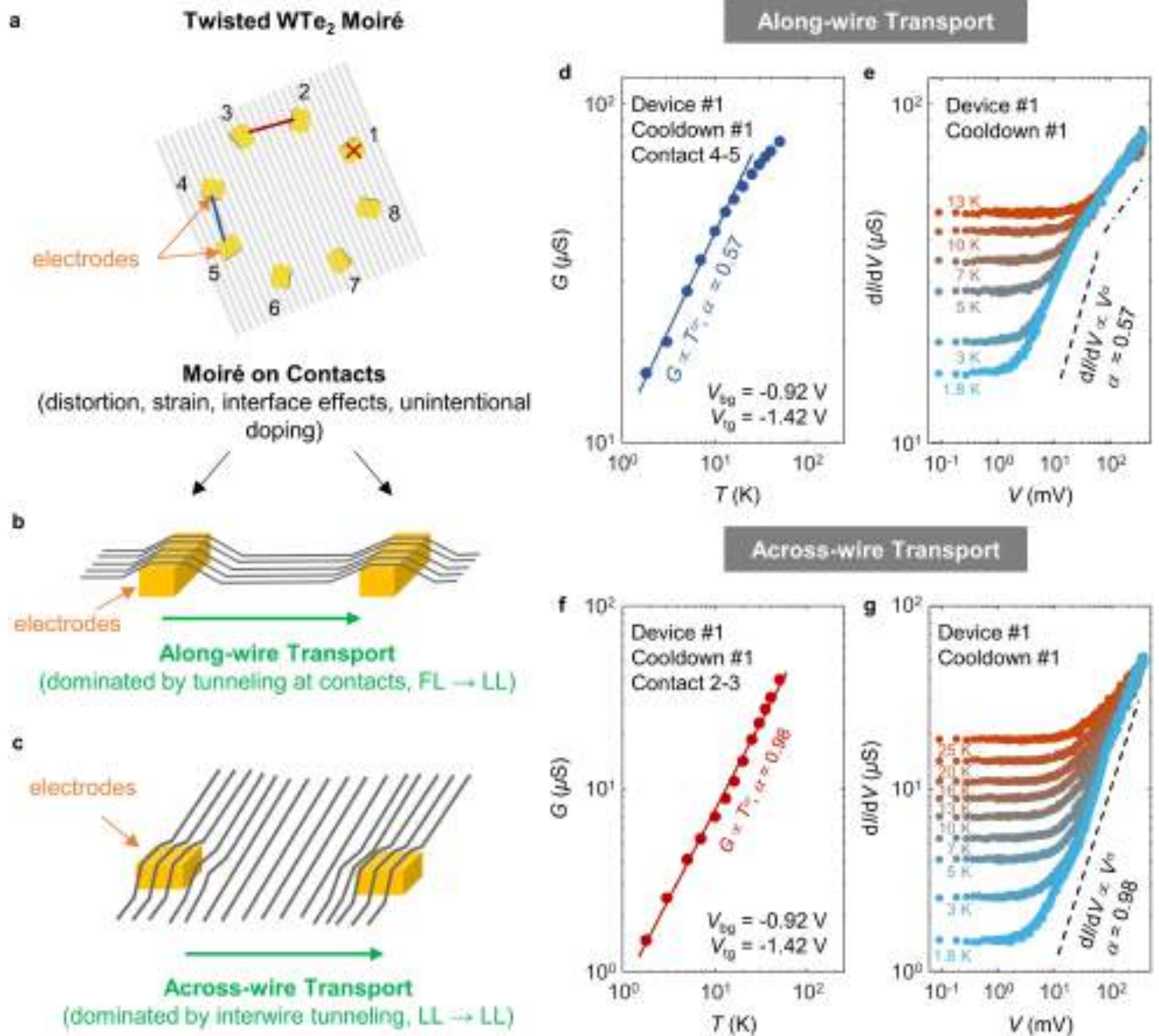


• Device #2 Cooldowns #1 $V_{\text{bg}} = -1.68 \text{ V}$; $V_{\text{g}} = -1.8 \text{ V}$; $n_0 = -5.0 \times 10^{12} \text{ cm}^{-2}$



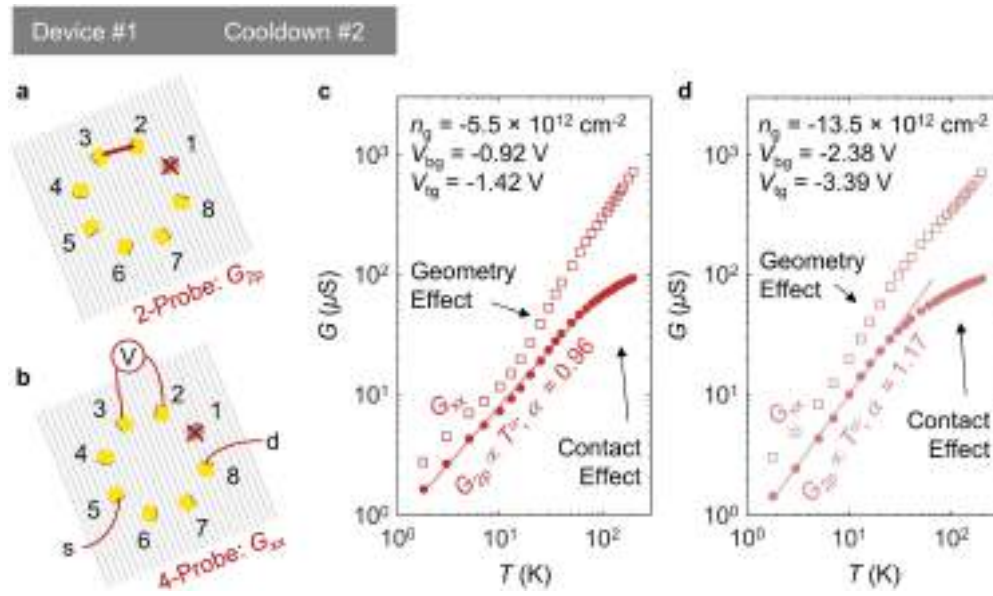
Extended Data Fig. 7 | Fitting to the differential conductance data based on the universal scaling formula. **a**, Raw data for the differential conductance measurements taken in device no.1 (replotted from Fig. 2d). **b**, 2D map of calculated root-mean-square error (r.m.s.e.) as a function of the fitting parameters, α and γ (see Methods for details). The best fit is obtained by finding

the minimal value of r.m.s.e. in this plot, i.e., $\alpha = 0.94$ and $1/\gamma = 9$. **c** & **d**, Scaled conductance as a function of scaled excitation by assigning $\alpha = 0.94$ in a log-log plot and log-linear plot. The dashed line indicates the fitting result given by the universal formula defined in the Method section. **e-h**, The same fitting plots for device no. 2, using the same raw data shown in Fig. 2f.



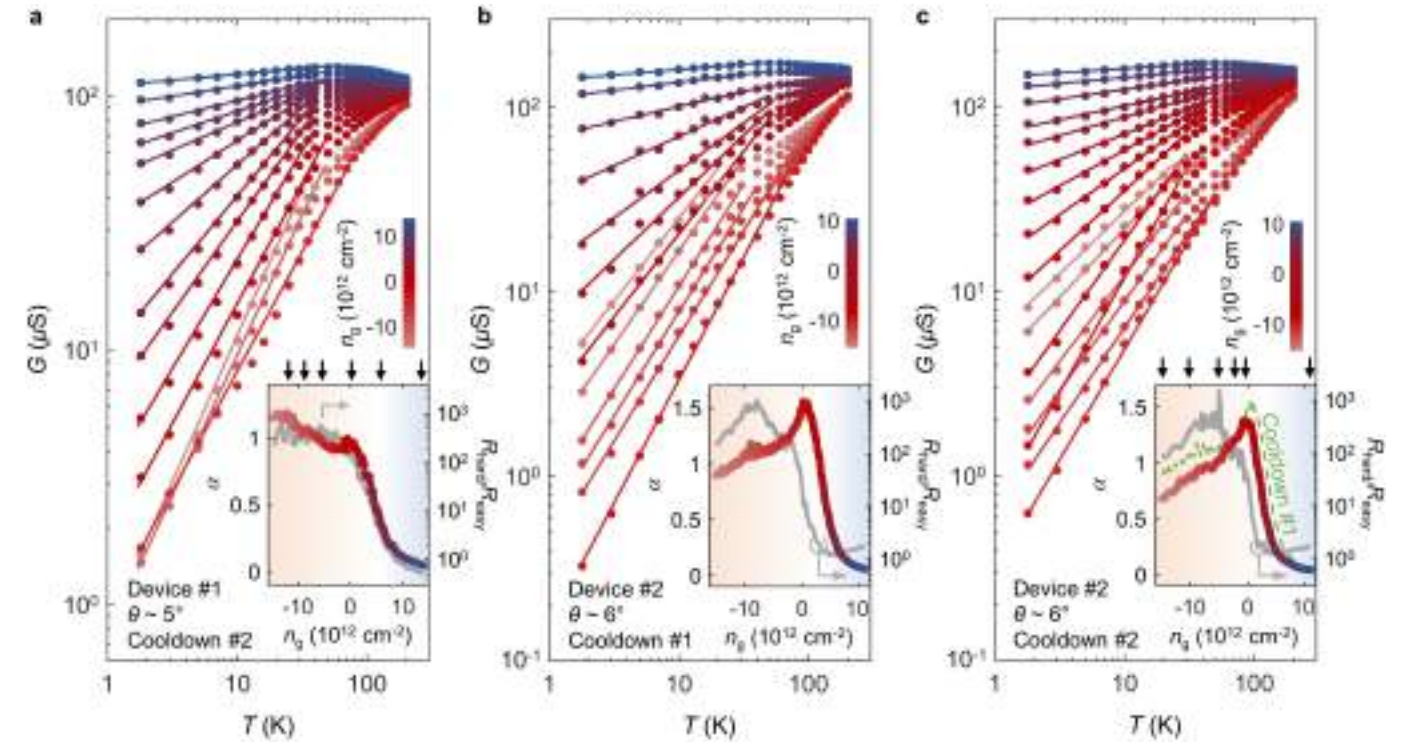
Extended Data Fig. 8 | Comparison between along-wire and across-wire transport. **a**, Illustration of tWTe_2 moiré stripes on the electrodes (top view). **b**, Illustration of transport along wires. At low T , the along-wire transport is dominated by contact resistance, i.e., tunnelling from the metal (FL) to the moiré wires (LL). **c**, Illustration of the across-wire transport, where the dominant resistance is due to interwire tunnelling in the stripe regime (i.e., LL to LL tunnelling). **d**, Along-wire two-probe conductance G as a function of T , plotted in log-log scale at a selected gate parameter. A power-law fit (solid line) to the low T data is shown. **e**, Differential conductance dI/dV taken under the along-wire transport configuration as a function of d.c. bias V at different T . The

dashed line indicates a power-law trend. The dot-dash line indicates a deviation from the trend at high bias. Note that distortions, strain, unintentional doping and other interface effects occur at the moiré in the contact regime, which could cause the deviation. **f** & **g**, the same plot for data taken from the across-wire transport (the same data as Fig. 2c, d), exhibiting a more robust power-law behaviour to higher bias and T . This can be understood as the dominant resistance in the across-wire transport comes from the tWTe_2 channel regime, which is more uniform compared to the contact regime. Data were taken from device no. 1 in cooldown no. 1.



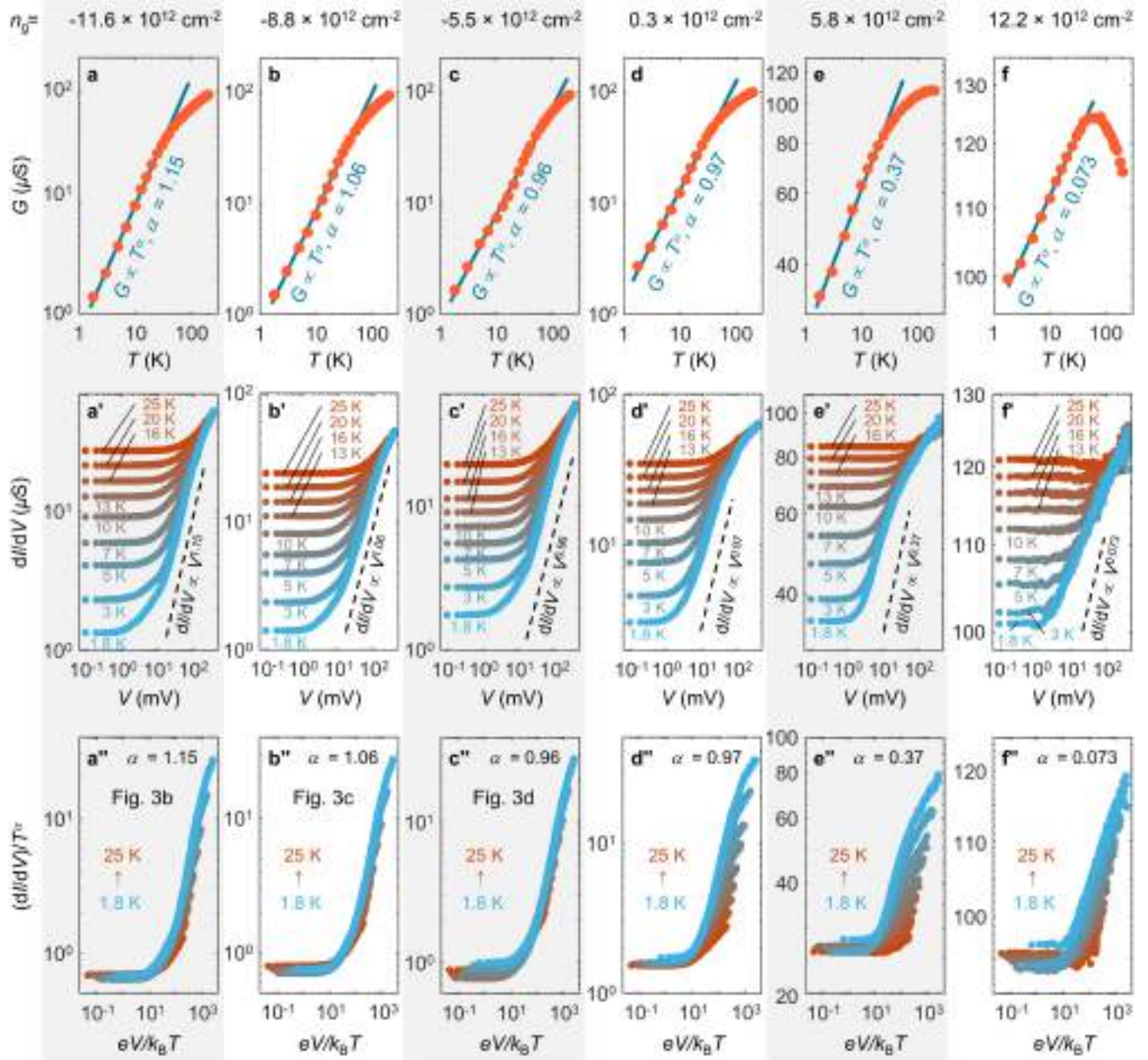
Extended Data Fig. 9 | Comparison of two-probe and four-probe measurements across the wires. Cartoon illustration of (a) two-probe (G_{2p}) and (b) four-probe (G_{xx}) configurations used for the measurements. **c and d**, G_{2p} and G_{xx} as a function of temperature taken in the hole-doped region ($n_g = -5.5 \times 10^{12} \text{ cm}^{-2}$ and $n_g = -13.5 \times 10^{12} \text{ cm}^{-2}$, respectively). At low T (1.8 K - 25 K) the trends of G_{2p} and G_{xx} both follow a power law and match well, demonstrating that the power law is intrinsic to the tWTe_2 channel. At high T , the two trends of G_{2p} and

G_{xx} deviate from each other, which can be understood as G_{2p} saturates due to contact resistances whereas G_{xx} is strongly affected by the temperature induced changes of anisotropy. The effective geometry factor, important for determining G_{xx} , changes as the sample is tuned from a strongly anisotropic phase at low T to an isotropic phase at high T . The main analyses in this paper are focused on the low T regime. The measurements were performed on device no. 1 in cooldown no. 2.



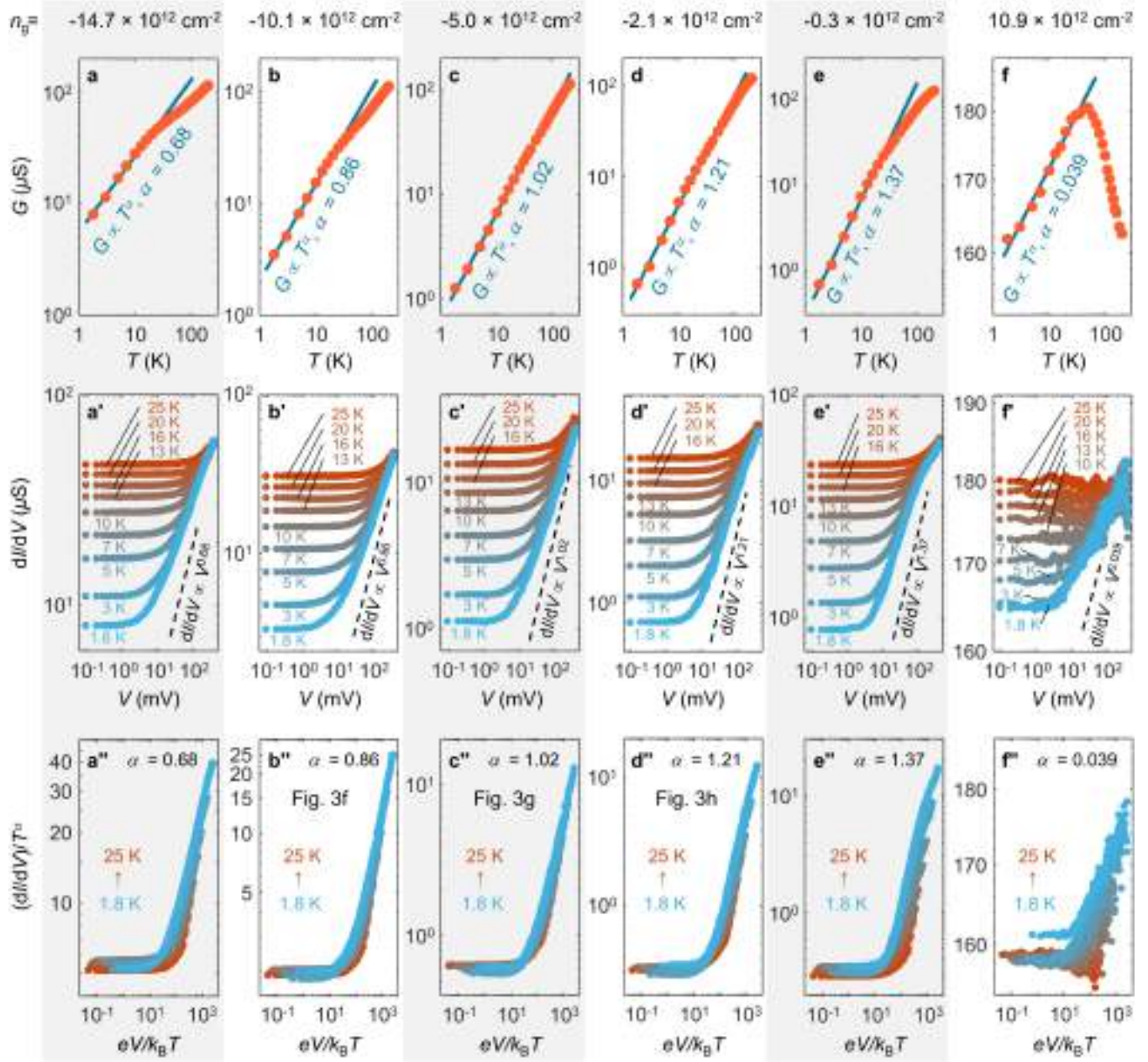
Extended Data Fig. 10 | Gate-tuned anisotropy cross-over. **a**, The across-wire two-probe conductance $G(T)$ displays a power-law relation ($G \propto T^\alpha$) for a wide range of doping for device no. 1 (cooldown no. 2). The colour of the data points encodes n_g , as shown in the colour bar. The solid lines are the power-law fittings, where the extracted exponent α is shown in the inset. The grey line replots the anisotropy ratio. **b**, The same plots for device no. 2 (cooldown no. 1). The grey line replots the anisotropy ratio shown in the inset of Fig. 1h. **c**, The

same plots for device no. 2 (cooldown no. 2). Note that data taken from two different cooldowns from device no. 2 shows qualitatively consistent results with only minor quantitative differences (dashed line in the inset of **c** is the exponent α replotted from the inset of **b** for comparison). Arrows to the insets in **a** and **c** indicate the selected n_g , at which the scaling analysis of the differential conductance is performed in Extended Data Figs. 11 and 12, respectively.



Extended Data Fig. 11 | Additional power-law scaling analysis for device no. 1 (cooldown no. 2). The corresponding n_g for each data set is indicated in the inset of Extended Data Fig. 10a. **a**, Temperature dependent cross-wire two-probe conductance $G(T)$ taken at the indicated n_g . The solid line is the power law fit. **a'**, Bias dependent differential conductance taken at the same n_g under different T . The dashed line indicates the power-law trend with the same exponent α extracted in **a**. **a''**, the same data in **a'**, but replotted as scaled

differential conductance $(dI/dV)/T^\alpha$ v.s. scaled bias $eV/k_B T$. Other panels are the same plots for different n_g . As seen in the plots, in the hole side (**a-c**) the data generally follows a power law very well, whereas near charge neutrality (**d**) and in the electron side (**e**), deviations start to develop at high bias. In the highly electron-doped region (**f**), dI/dV and G vary only a little bit ($\alpha \approx 0$) with changing both V and T , hence the behaviour is approximately ohmic. Data used for Figs. 3b-d are indicated in the lowest panel.



Extended Data Fig. 12 | Additional power-law scaling analysis for device no. 2 (cooldown no. 2). The corresponding n_g for each data set is indicated in the inset of Extended Data Fig. 10c. **a**, Temperature dependent across-wire two-probe conductance $G(T)$ taken at the indicated n_g . The solid line is the power law fit. **a'**, Bias dependent differential conductance taken at the same n_g under different T . The dashed line indicates the power-law trend with the same exponent α extracted in **a**. **a''**, the same data in **a'**, but replotted as scaled

differential conductance $(dI/dV)/T^\alpha$ v.s. scaled bias $eV/k_B T$. Other panels are the same plots for different n_g . As seen in the plots, in the hole side (**a-d**) the data generally follows a power law very well, whereas near charge neutrality (**e**), deviations start to develop at high bias. In the highly electron-doped region (**f**), dI/dV and G vary only a little bit ($\alpha \approx 0$) with changing both V and T , hence the behaviour is approximately ohmic. Data used for Figs. 3f–h are indicated in the lowest panel.